Forced Atmospheric Teleconnections During 1979-2014

Tao Zhang[1,2], Martin P. Hoerling[2], Judith Perlwitz[1,2], and Taiyi Xu[1,2]

[1]Cooperative Institute for Research in Environmental Sciences

University of Colorado

Boulder, Colorado

[2]NOAA Earth System Research Laboratory

Physical Sciences Division

Boulder, Colorado

2nd Revised version

(*Submitted to Journal of Climate*)

November 19, 2015

Corresponding author address:

Dr. Tao Zhang

NOAA/ESRL/PSD

325 Broadway, R/PSD1

Boulder, CO 80305

Email: tao.zhang@noaa.gov

Abstract

Forced atmospheric teleconnections during 1979-2014 are examined using a 50-member ensemble of atmospheric general circulation model (AGCM) simulations subjected to observed variations in sea surface temperatures (SST), sea ice and carbon dioxide. Three primary modes of forced variability are identified using empirical orthogonal function (EOF) analysis of the ensemble mean wintertime extratropical Northern Hemisphere 500-hPa heights. The principal component time series of the first and second modes are highly correlated with Nino3.4 and Trans-Niño (TNI) SST indices, respectively, indicating mostly tropical sources. Their impacts are largely confined to the Pacific-North American (PNA) sector. The leading mode describes the canonical atmospheric teleconnection associated with El Niño-Southern Oscillation (ENSO) resembling the Tropical/Northern Hemisphere pattern. The second mode describes a wavetrain resembling the classic PNA pattern resulting from atmospheric sensitivity to ENSO asymmetry and from sensitivity to a tropical precursor SST for ENSO development.

The third mode is characterized by a hemisphere-scale increasing trend in heights. Based on a comparison with 50-member coupled climate simulations it is argued that this mode is strongly related to radiatively forced climate change, while the other two forced teleconnections are principally related to internal coupled ocean-atmosphere variability.

A trend in the leading forced mode is related to ENSO-like decadal variability and dominates the overall observed 500 hPa height trend since 1979. These model results indicate that the trend in the first mode is due to internal variability rather than external radiative forcings.

1. Introduction

A long-term topic of research specifically related to climate predictability on a regional scale is to improve our understanding of the sensitivity of atmospheric circulation patterns to forcings, either to surface boundary conditions related to SST variability, or to external radiative forcing (and its associated surface boundary changes). Since recent decades have experienced a substantial increase in anthropogenically caused radiative forcing (IPCC 2013), a question of particular interest is how such forcing has driven variations in atmospheric circulation patterns. The goal of this study is to examine the structure of forced atmospheric teleconnections during Northern Hemisphere (NH) wintertime since 1979 and explore the relative roles of natural variations and external forcings.

Atmospheric teleconnections are a backbone for North American seasonal climate predictability, especially related to the well-known El Niño-Southern Oscillation (ENSO) phenomenon (Horel and Wallace 1981; Trenberth et al. 1998). Posed in the context of seasonal climate prediction, the issue is whether different North American wintertime conditions during El Niños can be anticipated on the basis of particular characteristics of the SST forcing. To tackle the question of whether ENSO could be used as predictor for seasonal climate, but especially to assess the relevance of ENSO diversity (Capotondi et al. 2015), numerous groups have conducted atmospheric general circulation model (AGCM) experiments over the last 30 years. Early experiments produced conflicting results, with Geisler et al. (1985) finding a single geographically fixed pattern of NH response to different patterns and magnitudes of warm tropical Pacific SSTs, and Palmer

and Mansfield (1986b) finding the 1982-83 El Niño forcing to induce a different atmospheric response than that associated with composite El Niño forcing. A strong dependency of responses upon the quality of a model's climatology was shown to exist (e.g. Palmer and Mansfield 1986a), and early results using coarse resolution climate models, often performed in idealized perpetual January mode, need to be interpreted with great caution.

A particular limitation that has plagued most modeling studies to date is the small ensemble sizes available from which to reliably extract the atmospheric responses for individual events. Thus, while Hoerling and Kumar (2000) found observed inter-El Niño variability in atmospheric circulation to be mostly unrelated to event-to-event differences in SSTs, the strength of their conclusion was undermined by their reliance on a relatively small 12-member ensemble. In a subsequent study, Hoerling and Kumar (2002) attempted to overcome the sampling problem by pooling simulations across four different models. The analysis of that multi-model ensemble revealed different response patterns depending on the characteristics of the tropical SST forcing, though much of the ENSO response manifested as a single spatial pattern. Whereas the larger ensemble size was evidently important for detecting additional atmospheric response patterns, the use of a multi-model approach introduced a new uncertainty in the interpretation. Recalling the lessons from early AGCM intercomparisons that revealed substantial model dependency in atmospheric responses, the possibility existed that the additional patterns found in Hoerling and Kumar (2002) were not signatures of a robust sensitivity. Furthermore, similar to the problem of potentially blurring sharper images of atmospheric responses to

ENSO when constructing an observed composite, the process of multi-model averaging may likewise obscure such patterns.

To overcome these limitations, Kumar et al. (2005) diagnosed an 80-member ensemble of AGCM historical runs using a single model. Their approach took advantage of a lagged ensemble of hindcast experiments that were being routinely conducted as part of the National Centers for Environmental Prediction (NCEP) seasonal forecast system. Applying empirical orthogonal function (EOF) analysis to the ensemble mean as in Hoerling and Kumar (2002), they found a leading atmospheric response pattern bearing considerable resemblance to the ENSO teleconnection pattern determined by Horel and Wallace (1981), but importantly explaining only about half of the magnitude in overall wintertime SST forced variability. The second response pattern exhibited strong zonal symmetry, whose time series was a trend during the 1980-2000 period of study. A third pattern again revealed strong regional variability, resembling some features of the third EOF pattern in Hoerling and Kumar (2002).

In sum, the two large ensemble model studies on SST-forced wintertime atmospheric circulations---one from a multi-model approach and a second from a particular model---indicate that a single teleconnection pattern resembling the ENSO composite determined by Horel and Wallace (1981) is indeed a robust and a dominant structure of the atmospheric circulation sensitivity to SST variability. To first-order, the magnitude and phase of this pattern can be understood to vary linearly with the magnitude and phase of ENSO-related tropical Pacific variations. This view of the atmospheric sensitivity

117 appears to account for roughly half of the wintertime NH variability in *SST forced*
118 *circulation variability*, though a greater portion over select regions such as the central
119 North Pacific. Higher-order patterns are less well understood, and currently lack clear
120 physical interpretation. For instance, the third leading pattern has been argued to be
121 linked to SST-driven teleconenctions during non-ENSO years in Hoerling and Kumar
122 (2002), while a similar pattern in Kumar et al. (2005) was believed to result form the
123 nonlinear atmospheric response to extreme opposite phases of ENSO. Also unresolved is
124 the physical explanation for a more zonally symmetric response pattern that appears to be
125 emergent in the time series of the forced solutions.
126
127 In so far as prior analyses have ended in either 1999 or 2000, it is important to update the
128 study to include a period in which external radiative forcing of climate has led to a
129 detectable effects on sea surface temperatures (IPCC 2013), though effects on
130 atmospheric circulation remain unclear. Further, it is important to understand whether
131 the dominant ENSO-related teleconnection pattern has changed during this period of
132 anthropogenic climate change.
133
134 This study addresses the nature and causes of boundary and externally forced modes of
135 extratropical Northern Hemisphere circulation variability over the recent period (1979-
136 2014) by utilizing large ensemble sized AGCM and coupled atmosphere-ocean model
137 simulations. The model and analysis methods are described in Section 2. Section 3 then
138 focuses on a physical interpretation of the December-February atmospheric sensitivity to
139 SST variability for the period 1979-2014 using both observations and model data. To

identify the role of different physical processes, both observed SST forced Atmospheric GCM simulations and radiatively forced coupled ocean-atmospheric GCM simulations are intercompared. Section 4 summaries our physical understanding of the forced atmospheric teleconnections during 1979-2014.

2. Data and Methods

a. Observed and model data

The characteristics of atmospheric variability are diagnosed from analysis of 500 hPa geopotential height fields conducted over the region 20°N-90°N. The study is of the Northern Hemisphere (NH) December-January-February (DJF) winter season and focuses on the recent 1979-2014 period. Estimates of the observed variability are derived from the National Centers for Environmental Prediction (NCEP)–National Center for Atmospheric Research (NCAR) reanalysis product (*Kalnay et al.* 1996). Analysis using other reanalysis products (ERA-Interim, Dee et al. 2011) is found to yield very similar results.

In order to determine the physical factors responsible for the observed 500 hPa height variability, we utilize atmospheric models (also called Atmospheric Model Intercomparison Project (AMIP) experiments) and coupled ocean-atmospheric models (also called Coupled Model Intercomparison Project (CMIP) experiments). For the former, the study primarily uses the National Centers for Environmental Prediction (NCEP) Global Forecast System model version 2 (GFSv2), the atmospheric component of the Climate Forecast System (CFS) version 2 (*Saha et al*. 2014). The model is run at

T126 horizontal resolution with 64 vertical levels, and forced with specified observed monthly varying sea surface temperatures, sea ice (Hurrell et al. 2008), and carbon dioxide concentrations for 1979-2014. Climatological values are specified for other greenhouse gases (e.g. CH4, NO2, O3, CFCs), aerosols, solar, and volcanic aerosols. A 50-member ensemble is conducted, each member forced identically but differing only by its initial atmospheric condition. The time evolving forced signal is derived from analysis of the 50-member ensemble average. To assess the robustness of key features in the GFS forced responses, we also diagnosis the time evolving signal from an 85-member ensemble of the European Center-Hamburg Max Planck Institute for Meteorology model 4.5 (ECHAM4.5; Roeckner et al. 1996) that spans January 1950 through February 2003. The model was run at T42 horizontal resolution with 19 vertical levels.

The signal in these AMIP experiments is further diagnosed to assess the component linked to changes in external radiative forcing, which may affect variability in 500 hPa heights through its influence on lower boundary conditions such as SSTs and sea ice (e.g. related to the ocean's response to long term global warming) and through direct atmospheric effects of changes in radiative forcing. To isolate the role of the external radiative forcing alone, we use a multi-model, 50-member ensemble of historical CMIP simulations. A 20-member ensemble is based on the Community Climate System Model, version 4 (CCSM4; Gent et al. 2011) whose atmospheric component is Community Atmospheric Model version 4 (CAM4; Neale et al. 2010), and a 30-member ensemble (Kay et al. 2015) is based on the Community Earth System Model version 1 (CESM1; Meehl et al. 2013) whose atmospheric component is CAM5 (Neale et al. 2012). Both

186 atmospheric components are run at ~1° horizontal resolution, with 26 vertical levels in
187 CAM4 and 30 levels in CAM5. Each member of these two coupled model runs is
188 similarly driven by changes in greenhouse gases, anthropogenic aerosols, solar and
189 volcanic aerosols, with starting from different initial conditions. The radiatively forced
190 atmospheric signals are derived from the ensemble-mean of 50 coupled runs, in order to
191 effectively separate the atmospheric response pattern from those arising from unforced
192 internal coupled ocean-atmospheric variability alone.
193
194 b. Diagnostic methods
195
196 The observed leading structures of the NH wintertime circulation patterns are obtained by
197 applying empirical orthogonal function (EOF) analysis to DJF seasonally averaged 500-
198 hPa heights for the 35 years of data during 1979-2014 period. The EOF analysis is based
199 on the covariance matrix for 20^{o}N-90^{o}N latitude bands, and a latitudinal weighting prior
200 to the EOF analysis is used. The EOF patterns are presented as regressions against the
201 principal component (PC) time series. Note that unrotated EOFs utilized here are
202 constructed to be both spatially and temporally uncorrelated to each other.
203
204 In this study, we determine the leading EOF modes of ensemble mean AMIP and CMIP
205 data, which allows us to isolate the forced signals. By comparison, leading EOF modes of
206 the observational record, or concatenated from individual ensemble members will involve
207 unforced internal atmospheric (or coupled ocean-atmospheric) variability.
208

209 In Appendix A, we provide a comparison of the patterns of the observed and GFS
210 simulated first three leading modes of variability of DJF 500 hPa geopotential heights.
211 This comparison demonstrates that the model is capable of capturing the observed two
212 leading modes of variability when concatenating the individual members of the GFS
213 AMIP simulations. These modes can also be largely reproduced in a long climatological
214 run driven with climatological lower boundary conditions, suggesting that the internal
215 atmospheric variability may play a dominant role in Northern Hemisphere wintertime
216 height variability. Section 3 will present the analysis of the fraction of the forced
217 atmospheric variability versus the total wintertime height variability to further quantify
218 the role of internal atmospheric variability.
219
220 As mentioned above, EOFs are calculated of the ensemble mean 500 hPa heights of the
221 AMIP and the CMIP data. For the AMIP model suite, the resulting patterns are of the
222 atmospheric sensitivity to the specified SST, sea ice, and radiatively forcing during 1979-
223 2014. These forcings commingle both internal ocean variations (e.g., ENSO) and
224 external variations related to anthropogenic climate change. For the CMIP model suite,
225 the resulting patterns are of the atmospheric sensitivity to specified radiative forcing
226 alone. While the coupled models produce internal ocean variations such as ENSO, these
227 are not temporally coherent among the individual ensemble members in the manner that
228 they are (by specification) in AMIP experiments. Thus, any SST-forced component of
229 height variability in the CMIP analysis will be principally related to the trend component
230 of global SST change that is coherent with the time series of radiative forcing.
231

232 We also carry out a composite analysis for extreme phases of the EOF patterns and
233 determine the associated anomaly patterns of 500-hPa heights, sea surface temperatures,
234 and North American surface temperature and precipitation.
235
236 **3. Results**
237 *a. Principal time-varying forced signals*
238
239 Figure 1 shows wintertime (DJF) 500 hPa height structures based on the two leading
240 EOFs of the ensemble-averaged AMIP simulations. Together these explain 79% of the
241 total boundary forced height variance. Contours in the left panels are the ensemble-mean
242 500 hPa heights regressed against each eigenvector's PC time series shown in the right
243 panels for 1979-2014.
244
245 A wave train having principal centers over the Pacific-North American sector describes
246 the height pattern maximizing variance in the extratropical NH forced solutions. Its
247 structure is well-known, resembling the observed height anomalies that are linearly
248 related to Nino3.4 SST variability (see Figure 3). This anomaly pattern, also called the
249 Tropical/Northern Hemisphere (TNH) pattern (Mo and Livezey, 1986), resembles the
250 configuration related to the leading EOFs of wintertime heights in observations (see
251 Figure A1). The time series for this leading mode shows clear co-variability with ENSO,
252 having positive polarity (i.e., the phase as shown in Fig. 1) during warm events (e.g.
253 1982/83, 1991/92, 1997/98, 2002/03, 2009/10) and negative polarity (i.e., the opposite
254 phase to that shown in Fig. 1) during cold events (e.g. 1988/89, 1998/99, 1999/2000,

255 2007/08, 2011/12). This pattern alone explains 56% of total boundary forced component
256 of extratropical NH wintertime height variability.
257
258 The height pattern associated with the second mode of forced AMIP solutions also
259 describes a wavetrain, but resembles the classic PNA pattern. Explaining 23% of the
260 total boundary forced height variability over the NH extratropics, its centers-of-action are
261 in spatial quadrature with the leading forced solution. Hartmann (2015) found a similar
262 mode of height variability by regressing winter 500 hPa heights onto the PC time series
263 of the second EOF of global 1979-2014 SST. This pattern arises from several
264 configurations of tropical Pacific SST variability. During strong El Niño events, both
265 PC1 and PC2 have large values, with the second EOF pattern acting to modify the overall
266 forced response by effectively shifting the centers-of-action of the first EOF pattern
267 eastward. In this sense, various magnitudes of PC1 and PC2 during warm events
268 describe so-called "flavors of El Niño" (e.g. Trenberth 1993; Hoerling and Kumar 2002;
269 Capotondi et al. 2015). The second EOF also describes the asymmetry in teleconnections
270 between El Niño and La Niña events, and is thus the spatial manifestation of the
271 nonlinearity in atmosphere responses to ENSO's opposite phases. Finally, this pattern
272 can arise in the absence of ENSO, being the dominant forced solution at times when
273 NINO3.4 SSTs are "ENSO-neutral". Thus, while the stronger amplitudes in the
274 corresponding PC-2 time series (Fig. 1, lower right) tend to occur during ENSO events
275 (e.g. 1982/83, 1991/92, 1997/98 warm events, and 1988/89, 1998/99, 2007/08, 2010/11,
276 2011/12 cold events), large projections also occur during several ENSO-neutral years
277 (1985/86, 1996/97, 2001/02, 2013/14). At such times, the forced solution is materially

278 different from the canonical ENSO teleconnection and has different impacts on North
279 American surface temperature and precipitation than the canonical ENSO signals, as
280 described further in section 3b.
281
282 We have utilized the large ensemble AMIP simulation from a different atmospheric
283 circulation model to repeat the analysis and found that the results in Figure 1 are robust
284 (Appendix B). This intercomparison indicates that the atmospheric sensitivities are
285 unique to the nature of the boundary forcing to which each atmospheric model was
286 subjected, rather than depending on the selection of a particular model. Our subsequent
287 analysis is thus based on the GFS data.
288
289 We diagnose the scatter relationship between the PC indices shown in Figure 1 and
290 various tropical Pacific SST indices to better understand the linkage between the first two
291 EOF modes and oceanic forcing during 1979-2014. The top panel of Fig. 2 shows the
292 relationship between the Nino3.4 standardized SST index, which is commonly used to
293 monitor ENSO, and the PC time series for the EOF1 500 hPa height mode (PC1). The
294 bottom panel of Fig. 2 shows the relationship between the Trans-Niño standardized SST
295 index (TNI), which measures the contrast in SSTs across the equatorial Pacific and helps
296 to capture the evolution of ENSO during its transition period (Trenberth and Stepaniak
297 2001), and the PC time series for the EOF2 500 hPa height mode (PC2). The correlation
298 between PC1 and Nino3.4 indices is 0.90, confirming that the height pattern associated
299 with the leading mode of forced AMIP solutions is the atmospheric expression of ENSO
300 forcing; the so-called canonical ENSO teleconnection. The correlation between PC2

301 index and TNI index is also high (0.74), indicating that the height pattern associated with
302 the second mode of forced AMIP solutions is linked to the evolution of ENSO.
303
304 To further confirm the linkage between the PC indices and tropical Pacific SST indices,
305 we have regressed the wintertime 500 hPa height from observations and the ensemble-
306 averaged AMIP simulations onto the Nino3.4 variability and the TNI index, respectively
307 (Figure 3). The results show that the model reproduces well the observed atmospheric
308 circulations associated with each ocean forcing. The similarities between the patterns in
309 Figure 3 and Figure 1 demonstrate that the height patterns associated with the first two
310 modes of forced AMIP solutions represent tropical SST forced teleconnections.
311
312 Whereas the overall temporal correlation between the PC1 and PC2 time series is zero,
313 there is nonetheless a strong physical relationship between these two as mentioned
314 previously. To explore the connection between the PC1 index and PC2 index, Figure 4
315 shows the scatter relationship between them. While there is no linear correlation between
316 these two PC time series by statistical construct, a nonlinear relationship is evident. For
317 the extremes values of PC1, PC2 is always positive. Further, the extreme positive
318 occurrences of PC2 arise solely in concert with strong PC1 states. Recalling that the
319 latter is a proxy for NINO3.4 SST variability, this result illustrates the nonlinearity of
320 atmospheric teleconnections through which the second response pattern is of the same
321 phase during both strong El Niño and La Niña events. This non-linear relation between
322 the PC1 and PC2 circulation patterns is mirrored by a similar non-linear relation between
323 the two leading EOF modes of tropical Pacific SSTs (Dommenget et al. 2013), with those

SST patterns being well described by the NINO3.4 and TNI indices, respectively. Affirmed hereby is that the difference between the oceanic expressions of El Niño and La Niña events is responsible for a difference in atmospheric teleconnections between ENSO's extreme states.

An interesting feature of the scatter relation is that the strong negative phases of PC2 occur almost exclusively when PC1 is near-normal, namely only during ENSO-neutral conditions during 1979-2014. It is unclear whether this is also true for the forced atmospheric teleconnections for other periods before 1979. Nonetheless, the result isolates the existence of a forced atmospheric teleconnection that is distinct from the well-known teleconnection occurring during mature ENSO conditions. The forced atmospheric circulation described by this PC2 is thus not a mere modifier of the canonical ENSO patterns, but can also exist as a unique stand-alone sensitivity pattern given particular states of the tropical ocean. As will be subsequently shown in composite analyses, this wintertime teleconnection emerges in the interlude between tropical SST evolutions from a recently completed La Niña to a subsequent El Niño. Within this transition toward El Niño, warm SSTs are often present in the tropical west Pacific and cool conditions are lingering in the tropical east Pacific, a pattern resembling the optimal structure for El Niño development 6-9 month later (Penland and Sardeshmukh 1995). These results indicate that there is a distinct atmospheric teleconnection (the negative phase of PC2) that accompanies such a precursor state to El Niño development.

b. Composite forced signals

Various characteristics of wintertime global climate associated with the leading forced atmospheric teleconnection are illustrated in Fig. 5. Shown are the composite patterns of Northern Hemisphere 500-hPa height, tropical SST and precipitation, North American surface temperature, and North American precipitation based on the upper and lower quintile of the PC1 time series during 1979-2014. Each composite consists of a 350-wintertime average constructed from the 7 strongest cases averaged across the 50-member model simulation.

For positive PC1 (Fig. 5, left), tropospheric circulation anomalies (top panel) resemble the Tropical/Northern Hemisphere (TNH) pattern (Mo and Livezey 1986). This positive phase occurs in concert with warm equatorial Pacific SSTs during the mature phase of El Niño (second panel). The well-known southeastward shift of low pressure from the Aleutians into the Gulf of Alaska and a development of anomalously high pressure over central Canada are part of a hemispheric wave train that brings above-normal temperatures to central and eastern North America (third panel) and above-normal rainfall to the southwestern United States (bottom panel). For negative PC1 values (Fig. 5, right), the global climate conditions are almost a mirror image, affirming the dominant linearity in atmospheric response to the extreme values of the Nino3.4 index. Some asymmetries are evident, however. For instance, the 500 hPa height anomaly centers are shifted 20-30° longitude west in the PC1 negative composite compared to PC1 positive composite, and resemble the Pacific-North American circulation pattern (Barnston and Livezey 1987) rather than the TNH pattern. Such asymmetry in the model's response is

371 consistent with observational evidence of nonlinearity in atmospheric teleconnections
372 associated with El Niño and La Niña (e.g. Hoerling et al. 1997).
373
374 The asymmetry in global climate conditions between extreme phases of PC1 is diagnosed
375 in Fig. 6, which presents the sum of composite anomalies for extreme positive PC1 (left
376 panels, Figure 5) and negative PC1 (right panels, Figure 5). The asymmetric height
377 pattern (top) is symptomatic of the aforementioned phase shift in teleconnections, a
378 structure very similar to the second EOF pattern of forced atmospheric teleconnections
379 (see Fig. 1). Consistent with the scatter relation of PC1 and PC2 time series, this result
380 again demonstrates a physical relationship between the two leading EOFs of forced
381 circulation, even though their respective time series are uncorrelated.
382
383 It is principally the difference in tropical forcing distinguishing strong El Niño from
384 strong La Niña events that causes the asymmetry in teleconnections related to PC1 (e.g.
385 Hoerling et al. 2001). Strong El Niños acquire larger SST amplitudes in the eastern
386 equatorial Pacific whereas strong La Niñas acquire larger SST amplitudes in the western
387 equatorial Pacific (Dommenget et al. 2013), the signature of which is captured in Fig. 6
388 (second panel). The resulting positive skew in the Nino3 index is further indication for
389 nonlinearity in SST forcing (Burgers and Stephenson 1999; An and Jin 2004; Zhang et al.
390 2009; Zhang and Sun 2014), which could be mainly caused by the extraordinary 1982-83
391 and 1997-98 El Niño events (Takahashi et al. 2011). Tropical convection is sensitive to
392 such differences, with strong El Niños exhibiting more enhanced rainfall in the eastern
393 Pacific, whereas strong La Niñas have less enhanced rainfall in the western Pacific. As

will be subsequently shown, this dipole in tropical forcing is not solely a residual of ENSO variance, but also arises during non-ENSO winters when the tropics can likewise act to force a teleconnection pattern resembling EOF2.

The asymmetric component of US climate conditions is physically consistent with those expected from the circulation asymmetry, the physical linkages of which have been examined in detail in Zhang et al. (2014). Here we add the interpretation that the skew in ENSO SST distributions implants a tendency toward non-Gaussian statistics in North American surface temperature. Over eastern North America especially, an outcome of asymmetry in the tropically forced teleconnection is that warm conditions, which appear during both strong El Niño and La Niña, would occur with greater frequency than expected from assumptions of normality (see Fig. 6, third panel). The asymmetric component of precipitation (Fig. 6, bottom) has a somewhat different interpretation. The widespread wet conditions over the West Coast result from the fact that the strong El Niño wet signal in central-northern California is appreciably more intense than the La Niña dry signal. Further, strong El Niños do not yield substantial wintertime dryness over Oregon/Washington, whereas those areas are considerably wet during La Niña. Overall, these indications for asymmetry in US climate impacts, originating from teleconnections driven by ENSO extremes, reveal a rectified effect comprised of a wetter far western North America and a warmer eastern North America, than would prevail in a climate lacking extreme ENSO variability.

Figure 7 presents the various characteristics of wintertime global climate associated with the second EOF of forced atmospheric teleconnection. Noteworthy here is that the composite maps for positive PC2 (left panels) are virtually identical to those associated with the asymmetric component of PC1 (cf. Figure 6). This follows directly from the scatter relation of the two PC time series (Fig. 4) where it was shown that most of the extreme positive states of PC2 occur in concert with the extreme PC1 positive and negative states. Thus, the simulation years comprising the composite of 7 extreme positive PC2 events, used to construct the left panels in Fig. 7, consist of a sum of extreme positive and negative PC1 cases from which the results of Fig. 6 were constructed. Physically, this positive PC2 phase and its associated global climate conditions are principally linked to ENSO.

On the other hand, the composite maps for negative PC2 (Fig. 7, right panels) are identified with SST forcing that is distinct from the mature states of ENSO. This phase of the teleconnection, consisting of anomalous low pressure over the central Pacific and anomalous high pressure along western North America, occurs in association with warm equatorial SST anomalies located slightly west of the Dateline, and cold SST anomalies along the equatorial east Pacific. The structure and phase of this teleconnection can be physically understood as resulting from tropospheric wave driving by enhanced convection initiated over the warm waters of the western Pacific, as demonstrated in dynamical model studies (e.g. Ting and Sardeshmukh 1993) and in idealized SST-driven climate simulations (Hoerling and Kumar 2002). The SST pattern is analogous to a pattern that is the precursor to El Niño development (e.g. Penland and Sardeshmukh,

1995). The principal North American impact of this SST pattern is dry/warm across the western United States. Vimont et al. (2001, 2003a,b) and Alexander et al. (2010) provided a physical mechanism, the so called "seasonal footprinting mechanism" (SFM) for such a precursor mode to induce El Niño, by which North Pacific atmospheric variability during the preceding winter affects tropical Pacific SST anomaly and the development of ENSO in the following year.

An application of this result concerning PC2 is that it clarifies and supports recent interpretations on causes for California drought in 2013-14, in particular the possible role of tropical forcing (e.g. Wang et al. 2014; Seager et al, 2014). We note that the largest negative PC2 loading since 1979 occurred during the 2013-14 winter (see Fig. 1) indicating that this non-ENSO, tropically forced teleconnection was a candidate mechanism in the severe drought and heat over California and the Far West. The results of AMIP simulations using 7 different climate models also have found a wave pattern of the type described by this negative phase of PC2 during winter 2013-14 (Seager et al. 2014)

c. Radiatively forced time-varying atmospheric signals and trends

Results in the previous sections indicate that the two leading forced teleconnections are strongly linked to interannual states of tropical Pacific SST forcing, either mature ENSO conditions or pre-cursor conditions preceding El Niño development. The PC1 time series also exhibits a downward trend during 1979-2014 (see Fig. 1), which may reflect an increased frequency of cold ENSO states in the recent decade compared to the first

462 decade, or may be suggestive of other low frequency forcing. The question arises in
463 particular whether the trend in this leading teleconnection during 1979-2014, or trends in
464 other manifestations of the model's forced responses, is symptomatic of atmospheric
465 sensitivity to time variations in external radiative forcing.
466
467 To address this question, we begin by diagnosing the third EOF of the AMIP ensemble
468 mean 500 hPa wintertime height variability (Fig. 8, top left). While explaining only 6%
469 of the variance in forced height variability (the first two EOFs explain 80% of the
470 variance), its pattern and temporal variability suggests a plausible physical interpretation
471 in a framework of global warming. First, EOF3 primarily describes a monopole structure
472 over the NH as a whole, a hemisphere-wide pattern distinct from the regional wave
473 structures of EOF1 and EOF2 that were each confined to the Pacific-North American
474 sector. Second, the PC3 time series (Fig. 8, top right) has a distinct upward trend that
475 describes a tendency for NH heights to rise since 1979 as would be expected from the
476 effects of anthropogenic greenhouse gas forcing.
477
478 The pattern of the third EOF and its temporal trend of the PC alone are however not
479 sufficient for a physical interpretation related to climate change because this higher mode
480 of variability is constrained by temporal and spatial orthogonality in relation to the
481 leading two modes. Therefore, we utilize a 50-member ensemble of CMIP simulations.
482 Recall that the only forcing that is temporally synchronized among every CMIP model
483 realization is anthropogenic greenhouse gases, anthropogenic aerosols, solar and volcanic
484 variability. The CMIP EOF1 regression pattern and the related PC are shown in the

485 bottom panels of Fig. 8. The leading 500 hPa height pattern associated with such forcing
486 describes a hemisphere-wide monopole whose time series consists of an upward trend.
487 These characteristics reproduce many features of the space-time variability of EOF3 from
488 the AMIP analysis, including also the magnitude of variations, which are typically about
489 5 meters in both. Specifically, the CMIP EOF1 has a strong spatial congruence (r=0.79)
490 with the EOF3 of the AMIP model. By comparison, there is no appreciable spatial
491 agreement of the externally forced solution with the EOF1 and EOF2 of the AMIP model
492 (r=0.40 and r=0.03, respectively). We also compared the root mean square (RMS) of the
493 magnitude of three EOF patterns from AMIP analysis with that of EOF1 pattern from
494 CMIP simulations. The results show that compared to EOF1 and EOF2 modes, the
495 magnitude of EOF3 pattern from AMIP analysis is much closer to that of EOF1 pattern
496 of CMIP simulations. The results, from several lines of evidence, thus indicate radiative
497 forcing to be instrumental in understanding the third EOF of AMIP responses.
498
499 Considering the trend in the leading EOF of the AMIP response, our interpretation is that
500 this is unlikely a symptom of sensitivity to time variations in external radiative forcing.
501 We have calculated the ensemble mean of the leading EOFs derived from the individual
502 historical coupled simulations (See Appendix C). The ensemble mean pattern is spatially
503 similar to the leading EOF (EOF1) of the AMIP response (and also EOF1 of observed),
504 and captures the dominant structure of the ENSO teleconnection (see Fig. C1, top left).
505 However, unlike the time series of the AMIP EOF1, the time series of the EOF1 of the
506 average of individual coupled runs exhibits no appreciable trend (Fig. C1, top right).

These results indicate that external radiative forcing has no significant effect on the trend in the leading ENSO teleconnection pattern, in the models studied herein.

We also note that the time series of EOF1 derived from individual coupled model samples can have a strong positive (or negative) trend, the magnitude of which was found to be at least as large as the trend in the AMIP EOF1 (not shown). There is thus a large range of internal variability on multi-decadal time scales in the coupled models. This result, together with the evidence that the leading ENSO teleconnection is not materially affected by external radiative forcing during 1979-2014, supports an interpretation that the trend in the forced ENSO teleconnection of AMIP response has resulted principally from internal coupled variability. We can not exclude the possibility that ENSO itself may be changing in response to external forcing, although CMIP model simulations do not show consensus on the response of ENSO variability to climate change (Guilyardi 2006; Collins et al. 2010; Stevenson 2012; Kim et al. 2014). Furthermore, long coupled runs for pre-industrial conditions yield decadal to centennial modulations of ENSO (Wittenberg, 2009; Yeh et al. 2011), and thus one would expect corresponding multi-decadal variations in forced atmospheric teleconnections. Due to the high correlation between AMIP PC1 time series and a N3.4 index, it is quite plausible that the trend in AMIP EOF1 is symptomatic of such internal ENSO-like multi-decadal variability.

How large is the contribution of radiative forcing changes to the total circulation variability during 1979-2014? To address this question, Figure 9 presents the ratio of wintertime 500 hPa height variances calculated for the AMIP (top) and CMIP (bottom)

530 simulations. The total variance, which appears in the denominator of the ratio,
531 commingles forced variations and internally driven variations (either of the atmosphere
532 alone in AMIP or of the coupled ocean-atmosphere in CMIP). Its magnitude and spatial
533 pattern is very similar in the two model configurations (not shown). The forced
534 components, which appear in the numerator of the ratio, are very different however. The
535 forced component in CMIP represents the physical effects of external radiative forcing
536 arising from both the atmosphere's sensitivity to lower boundary changes (e.g., a broad
537 oceanic warming in response to increasing radiative forcing), and the direct effects of
538 radiative forcing on the atmosphere alone. As shown in the lower panels of Fig. 9, this
539 forced component is a small fraction of total variability, generally less than 5% poleward
540 of 30°N. A similar pattern of variance ratios is found when using the AMIP EOF3 forced
541 signal in the numerator (Figure 10), thus providing further evidence that radiative forcing
542 is unlikely to be a substantial factor in driving year-to-year variability of wintertime
543 extratropical circulation.
544
545 The results support the interpretation that radiative forcing has limited explanatory power
546 for height variations during 1979-2014. As a consequence, knowledge of the time series
547 of radiative forcing offers little potential for predicting the overall interannual variability
548 in wintertime atmospheric circulation.
549
550 By contrast, the forced component in AMIP incorporates the atmosphere's sensitivity to
551 the particular history of observed ocean variability, including especially ENSO variations
552 observed during 1979-2014, in addition to the aforementioned physical effects related to

553 radiative forcing. Strong atmospheric forcing by the particular history of SST variations
554 explains why the ratio of variances in the AMIP simulation, shown in the upper panels of
555 Fig. 9, is much larger than in CMIP. The magnitude is nearly an order of magnitude
556 greater in portions of the Pacific-North American region in AMIP versus CMIP. It is in
557 that region especially where atmospheric responses to observed tropical Pacific SST
558 variations that occurred during 1979-2014 dominates the overall boundary forced
559 variance in AMIP.
560
561 The results of the AMIP analysis thus indicate the particular history of tropical Pacific
562 SST variability to be key for understanding the nature of forced atmospheric
563 teleconnections during 1979-2014. These SST forcings render appreciable explanatory
564 power for PNA-sector height variations, and knowledge of the time series of ENSO and
565 related internal states of the tropical Pacific Ocean offers substantial potential
566 atmospheric predictability, whereas the radiative forcing alone explains little variance.
567 The same distinction does not hold elsewhere. Both AMIP and CMIP variance ratios are
568 small over the North Atlantic, Europe, and Asia. In those regions, the results of Fig. 9
569 indicate that neither radiative forcing alone, nor the additional knowledge of the sequence
570 of observed SST variations, contributes appreciably to circulation variability thereby
571 limiting overall interannual predictability.
572
573 Figure 11 reveals that it is principally EOF1, and not EOF3, that explains most of
574 wintertime NH 500 hPa height trend occurring in the AMIP ensemble. The left panels of
575 Fig. 11 compare the 1979-2014 trend in 500 hPa heights associated with EOF1 (top) to

576 the total AMIP ensemble mean trend (bottom). These are almost indistinguishable in
577 pattern and magnitude indicating that irregularity in Nino3.4 SST variability during this
578 period, with greater frequency of La Niña events in later years, is mainly responsible for
579 trend in forced circulations. Incorporating the trend contribution from EOF3 doesn't
580 materially change the trend derived from EOF1 alone (see Fig 11, top right). Most of the
581 regional patterns of NH wintertime height change since 1979 thus appear unrelated to the
582 radiative forcing time series, consistent with the findings of Perlwitz et al. (2015). We
583 note, however, that the possibility can not be excluded that the CMIP models have biases
584 relevant to this interpretation. In particular, a post-1979 trend toward cold states of the
585 tropical eastern Pacific is a very low probability of CMIP models (e.g. Hoerling et al.
586 2010), which could indicate a different sensitivity to radiative forcing in nature in
587 addition to the more likely possibility that this has been an extreme case of internal
588 variability.
589
590 It is instructive to compare the AMIP ensemble mean height change since 1979 with the
591 observed height change pattern. Agreement is strong, principally over the North Pacific
592 where both indicate trends toward increased anticyclonic circulation (compare bottom
593 panels of Fig. 11). The agreement over the North Pacific is not surprising given the high
594 signal-to–noise ratio for interannual variability found in the AMIP simulations (Fig. 9)
595 Physically, this observed trend toward anticyclonic circulation is consistent with
596 atmospheric sensitivity to a change in ENSO statistics, with La Niña events more
597 common during 1999-2014 while El Niños dominated the 1980s and 1990s. The ratio of
598 variance indicates that detectability of such a North Pacific circulation change in

observations is expected to be high, and thus the fidelity of the simulated trend is not surprising. The interpretation is not particularly dependent on whether one interprets the change in Pacific basin SSTs during 1979-2014 as symptomatic of ENSO-like interdecadal variability (e.g. Zhang et al. 1997), or indicative of a Pacific decadal climate oscillation (e.g. Mantua et al. 1997). By contrast, an observed circulation trend over the North Atlantic basin, which projects onto a negative phase of the North Atlantic Oscillation (NAO), is not reconcilable with forcing in the AMIP (or CMIP) simulations. Here the ratio of variances analysis showed forcing to be ineffective in driving interannual variability of atmospheric circulation, and it is plausible that the recent trend toward the negative NAO phase is largely a symptom of internal atmospheric variability (see also Perlwitz et al. 2015).

4. Summary and discussion

In this study, the forced modes of NH winter 500-hPa heights for the period of 1979 to 2014 were determined by utilizing a 50-member ensemble of atmospheric general circulation model (GFSv2) simulations and by carrying out an EOF decomposition of the ensemble mean 500-hPa height anomalies. We identified three main modes that together explain about 85% of the forced variability of 500 hPa wintertime height variability poleward of 20^{o}N.

The first two leading modes, which together explain 79% of the forced height variance, are associated with tropical SST forcing. The first EOF describes the canonical tropical-

622 extratropical teleconnection pattern (TNH) that has historically been interpreted as the
623 linear response to ENSO's extreme opposite phases. That is, the positive (negative) phase
624 (indicated by PC values) of the first EOF mode is linked to the response during warm
625 (cold) ENSO events. A high correlation (~0.9) between the principal component of this
626 EOF and the Nino3.4 index therefore exists. The second forced mode describes the
627 classic PNA circulation pattern, and is closely linked to the Trans-Nino index—a
628 correlation coefficient of 0.74 is found between the TNI and the principal component
629 time series of this mode.
630
631 Our analysis of the scatter relationship between the PCs of these first and second AMIP
632 modes, together with composite analyses, offers new insights into the physics of this
633 second forced teleconnection pattern. Its positive phase is shown to be an expression of
634 the asymmetry in ENSO teleconnections between their extreme opposite warm and cold
635 phases. This arises most strongly during the intense El Niño events of 1982/83 and
636 1997/98. Consistent with this asymmetry in ENSO teleconnections, we demonstrate that
637 wet conditions occur over far western North America and warm conditions over eastern
638 North America during both strong ENSO phases. Its negative phase is shown to be an
639 expression of atmospheric responses that occur mostly during ENSO-neutral winters
640 when a distinctive tropical SST pattern having warmth in the far western Pacific and
641 coolness in the far eastern Pacific can arise. This forcing resembles a precursor state that
642 often is followed by a mature El Niño event in 6-9 months. The principal climate impact
643 related to this forced teleconnection is an anomalously dry and warm climate across the
644 western United States.

It should be noted that these two leading teleconnection modes are not particularly dependent upon just two strong warming events (1982/1983 El Niño and 1997/1998 El Niño) or the 1979-2014 period. We have recalculated the AMIP EOFs of 500 hPa heights by considering two separate periods (1984-1997 and 1999-2014), neither of which includes these two strong events. The two leading EOFs emerge with little change in structure in these sub-periods, with the principal difference being a reduced explained variance of EOF2. Based on the available ECHAM4.5 simulations spanning 1950-2003, we have compared the leading two EOF patterns of that model's forced teleconnections during 1950-1978 to the subsequent period, and found little appreciable difference. In light of the high consistency in the first two EOFs among models and for different periods of analysis, it is suggested that our analysis of the 1979-2014 period is robust and is likely representative of a longer period of study.

By comparing the AMIP (GFSv2) EOF analysis results with CMIP (CCSM4 and CESM1) EOF analysis we argue that the third AMIP EOF mode is associated with radiatively forced climate change. This mode explains 6% of the forced variance in the AMIP ensemble mean and is thus much weaker than the contribution from the first two modes. The time series of this third EOF consists mostly of a trend pattern that primarily describes increasing geopotential heights in the Northern Hemisphere, consistent with a global warming signal. However, a trend in the PC time series of AMIP EOF1 is found to dominate the overall trend in the AMIP ensemble mean and observations during 1979-2014. Our analysis therefore suggests that the observed trend of winter heights during the

668 recent period is more determined by the decadal variability associated with low frequency
669 fluctuations in ENSO than by the external radiative forcing.
670
671 Our results have some relevance to the question of the atmospheric sensitivity to different
672 "Faces of El Niño" (e.g. Capotondi et al. 2015). Studies have shown that, distinct from
673 the canonical El Niño with warming in the eastern equatorial Pacific ocean (EP- El
674 Niño), a different expression of SST warming confined to the central Pacific region also
675 occurs. This latter warming pattern is referred to variously as the central Pacific (CP) El
676 Niño (Yu and Kao 2007; Kao and Yu 2009), Date Line El Niño (Larkin and Harrison
677 2005), El Niño Modoki (Ashok et al. 2007), or warm pool El Niño (Kug et al. 2009). The
678 central Pacific events have been interpreted as a nonlinear manifestation of the canonical
679 ENSO (Takahashi et al. 2011; Dommenget et al. 2013; Johnson 2013). The question has
680 been explored whether these two types of El Niño have different impacts on wintertime
681 extratropical climate (e.g. Yeh et al. 2009; Yu et al. 2012). Our analysis indicates that
682 there indeed exist additional forced atmospheric response patterns beyond a single
683 canonical (linear) ENSO response, though the EOF approach is not suitable to clarifying
684 the different structures of atmospheric responses across a continuous spectrum of El Niño
685 warming patterns. A better understanding of these different structures is a subject of
686 ongoing research.
687
688 Future work is also needed to better understand the predictive value implicit in the
689 knowledge of these forced teleconnections for US climate. For instance, is the potential
690 predictability implied by the three leading teleconnections being realized in current

691 climate prediction systems? What is the contribution of the different modes to US
692 seasonal forecast skill? And, at what lead times are the different forcings of these
693 teleconnections themselves predictable?
694
695 The PC time series of the forced teleconnections describe distinct "forecasts of
696 opportunity". Some are well known, such as the strong El Niño events in 1982-83 and
697 1997-98. Others are less well known, and deserving additional study. For example,
698 during winter of 2013-14 the negative phase of the second mode was strongly enhanced,
699 an important indicator for a possible role of tropical forcing in that winter and its impact
700 on California precipitation deficits and high temperatures during that winter (see also
701 Seager et al. 2014). Hartmann (2015), using the same model data, also identified a
702 coherent atmospheric teleconnection for 2013-14 that includes a warm West-cold East
703 surface temperature dipole.
704
705 Our analysis focuses on the 1979-2014 period, which may not very well contain all the
706 "Faces of ENSO", among other modes of SST variations to which forced teleconnections
707 may be sensitive. In addition, the time-dependent volcanic aerosols forcing is not
708 included in the present AMIP simulations. In a next step we plan to carry out a parallel
709 analysis of large historical simulations spanning the post-1900 period using a large
710 ensemble AMIP and large ensemble CMIP data set, in which identical AGCM
711 components forced with the changes in volcanic aerosols and anthropogenic greenhouse
712 gases are involved. This may provide a clearer separation of the sensitivity of forced

atmospheric teleconnections arising from external forcing alone versus from the additional effect of the particular trajectory in observed SST conditions.

APPENDIX A

Comparison of leading modes of variability of 500hPa heights in reanalysis and GFS model simulations

The EOF patterns between the reanalysis data and GFS model simulations are compared to examine the model fidelity in simulating the leading modes of variability of Dec-Feb mean 500hPa heights. Figure A1 (left panels) shows the regression patterns corresponding to the first 3 EOFs of reanalysis data, which explain a combined 54.8% of the wintertime height variability poleward of 20°N. The same EOF procedure is applied to the climate simulations. In this application, we concatenate the individual members of the AMIP simulations, which for the GFS data consist of 1750 winter seasons. Figure A1 (middle panels) shows the regression patterns corresponding to the first 3 EOFs of GFS simulations, which explain a combined 46.8% of the model's wintertime height variability poleward of 20°N. The model is seen to replicate the leading observed pattern of 500 hPa height variability which consists of a prominent wave train over the Pacific-North American region. The observed second EOF pattern is likewise part of the model's leading modes of variability, though ranked third in its EOF decomposition and explaining less overall height variance. We note that there exists considerable sampling variability in the EOF rankings and detailed structures based on separate samples of only 35 winters (not shown). We have quantified the range of pattern similarity between

737 model simulations and observations for the first 3 EOFs. The EOF1 pattern congruence
738 between individual members of the AMIP simulations and observations based on 35
739 winters ranges from 0.59 to 0.95. However, the range of EOF2 and EOF3 pattern
740 congruence is more scattered, with values from 0.00 to 0.89 for the former and from 0.02
741 to 0.88 for the latter. This large uncertainty is expected because of the considerable
742 sampling variability in the EOF rankings in the model simulations, in addition to the
743 possible model biases.
744 The leading patterns of the GFS 500-hPa height variability can be largely reproduced in a
745 climate simulation having no interannual variability in boundary conditions or external
746 radiative forcing. A 100-yr long climatological run of GFS has been performed using
747 repeating seasonal cycle SSTs and carbon dioxide concentrations corresponding to the
748 mean of 1979-2014. Figure A1 (right panels) shows the regression patterns
749 corresponding to the first 3 EOFs of this climatological run, which explain a combined
750 43.8% of the wintertime height variability poleward of 20°N. The spatial structures are
751 very similar to the AMIP version of the model, and it is evident that internal atmospheric
752 variability is a major source of NH wintertime height variability.
753
754
755 APPENDIX B
756 **Comparison of forced modes of variability between GFS and ECHAM4.5 models**
757 The robustness of the boundary forced atmospheric circulation sensitivities shown in Fig.
758 2 is evaluated by repeating the EOF analysis using different model data. Important in
759 such intercomparison is the use of large-sized ensemble simulations so as not to confound

760 forced patterns with internal atmospheric variability that may dominate an EOF analysis
761 based on small-sized ensembles. We have therefore used the data from an 85-member
762 ensemble of similarly designed AMIP experiments derived from the ECHAM4.5 model
763 (Roeckner et al. 1996; data provided by IRI, see
764 http://iridl.ldeo.columbia.edu/SOURCES/.IRI/.FD/.ECHAM4p5/.History/.ensemble85/).
765 Differences in parameterizations and spatial resolutions (e.g., ECHAM4.5 is run at T42
766 scale) permit a meaningful evaluation of whether these large spatial modes of
767 atmospheric sensitivity derived from GFS data are robust to model formulation. Figure
768 B1 compares the height structures corresponding to the first two EOFs of wintertime 500
769 hPa heights for a common simulation period of 1979-2003. The spatial patterns of the
770 models' corresponding EOFs are very similar (spatial correlation exceeds 0.9 over the
771 map domain), as are the temporal variations in their PC time series (temporal correlation
772 of forced solutions exceeds 0.9 during 1979-2003). This intercomparison reveals that the
773 atmospheric sensitivities do not depend on the selection of a particular model. They are
774 more determined by the nature of the boundary forcing used for each atmospheric model
775 instead.
776
777
778 APPENDIX C
779 **The leading mode of variability of 500hPa heights in individual coupled runs**
780
781 The leading EOF (EOF1) mode of variability of winter (DJF) season 500-hPa heights in
782 50 individual coupled runs (30 CESM1 runs and 20 CCSM4 runs) is examined to explore

783 the role of external radiative forcing on the trend in the leading ENSO teleconnection
784 pattern. Figure C1 (bottom) provides a validation of the realism of the coupled models, in
785 so far as this "recurrent" EOF1 pattern of each member is spatially very similar to the
786 observed EOF1 height pattern shown in Figure A1 (The EOF1 pattern congruence
787 between individual coupled runs and observations ranges from 0.66 to 0.92 and the
788 dominant congruence values are within 0.8~0.9). The ensemble mean of EOF1 pattern
789 averaged over 50 individual coupled runs has a strong spatial congruence (r=0.88) with
790 observations (Figure C1, top left), and the time series of this mode of coupled variability,
791 on average, has no significant trend during 1979-2014 (Figure C1, top right). The results
792 indicate that external radiative forcing has no significant effect on the trend in the leading
793 ENSO teleconnection pattern. We also note that the time series of EOF1 from the
794 individual coupled model samples can have a strong positive (negative) trend, ranging to
795 as much as 1.51 (and -1.36) standardized units, showing a large range of internal
796 variability effects on this multi-decadal time scale. This result supports the argument that
797 the trend in EOF1 pattern of AMIP (GFSv2) 500-hPa height (see Figure 1 and Figure 11
798 top left) is not appreciably due to climate change forcing. Instead, the trend in this AMIP
799 EOF1 is a symptom of internal variability.
800

Acknowledgments

This work was supported by grants from NOAA's Climate Program Office. We acknowledge NCAR's CESM1(CAM5) Large Ensemble Community Project for carrying out the large CESM1 ensemble. We wish to thank Xiaowei Quan for carrying out the large CCSM4 ensemble, and Jon Eischeid for his technical support**.** We also thank three anonymous reviewers for their constructive comments that helped to improve the paper.

References:

Alexander, M. A., D. J. Vimont, P. Chang, and J. D. Scott, 2010: The impact of extratropical atmospheric variability on ENSO: Testing the seasonal footprinting mechanism using coupled model experiments. *J. Climate*, **23**, 2885–2901.

An, S-I., and F-F. Jin, 2004: Nonlinearity and asymmetry of ENSO. *J. Climate*, **17,** 2399–2412.

Ashok, K., S. K. Behera, S. A. Rao, H. Weng, *and* T. Yamagata, 2007*:* El Niño Modoki and its possible teleconnection*, J. Geophys. Res.*, 112*, C11007, doi:*10.1029/2006JC003798.

Barnston, A. G., and R. E. Livezey, 1987: Classification, seasonality, and persistence of low-frequency atmospheric circulation patterns. *Mon. Wea. Rev.*, **115,** 1083–1126.

Burgers, G., and D. B. Stephenson, 1999: The "normality" of El Niño. *Geophys. Res. Lett.*, **26,** 1027–1030.

Capotondi, A., and Co-authors, 2015: Understanding ENSO Diversity. *Bull. Amer. Meteor. Soc.*, **96**, 921–938. doi: http://dx.doi.org/10.1175/BAMS-D-13-00117.1

Collins, M., and Coauthors, 2010: The impact of global warming on the tropical Pacific Ocean and El Niño. *Nat. Geosci.*, **3**, 391–397.

Dee, D. P., and 35 co-authors, 2011: The ERA-Interim reanalysis: Configuration and performance of the data assimilation system. *Quart. J. R. Meteorol. Soc.*, **137**, 553-597. DOI: 10.1002/qj.828.

Dommenget, D., T. Bayr, and C. Frauen, 2013: Analysis of the non-linearity in the pattern and time evolution of El Niño Southern Oscillation. *Climate Dyn.*, **40**, 2825–2847.

836 Geisler, J. E., M. L. Blackmon, G. T. Bates, and S. Munoz, 1985: Sensitivity of January
837 climate response to the magnitude and position of equatorial Pacific sea surface
838 temperature anomalies. *J. Atmos. Sci.*, **42,** 1037–1049.
839 Gent, P., and Coauthors, 2011: The Community Climate System Model version 4. *J.*
840 *Climate*, **24**, 4973–4991.
841 Guilyardi, E., 2006: El Niño-mean state-seasonal cycle interactions in a multi-model
842 ensemble. *Climate Dyn.,* 26, 329–348.
843 Hartmann, D. L., 2015: Pacific sea surface temperature and the winter of 2014. *Geophys.*
844 *Res. Lett.,* **42**, doi:10.1002/2015GL063083.
845 Hoerling, M. P., and A. Kumar, 2000: Understanding and predicting extratropical
846 teleconnections related to ENSO. *El Niño and the Southern Oscillation: Multi-Scale*
847 *Variability, and Global and Regional Impacts,* H. Diaz and V. Markgraf, Eds.,
848 Cambridge University Press, 57–88.
849 Hoerling, M. P., and A. Kumar, 2002: Atmospheric response patterns associated with
850 tropical forcing. *J. Climate*, **15,** 2184–2203.
851 Hoerling, M. P., A. Kumar, and M. Zhong, 1997: El Niño, La Niña, and the nonlinearity
852 of their teleconnections. *J. Climate*, **10,** 1769–1786.
853 Hoerling, M. P., A. Kumar, and T.-Y. Xu, 2001: Robustness of the nonlinear
854 atmospheric response to opposite phases of ENSO. *J. Climate*, **14**, 1277-1293.
855 Hoerling, M. P., J. Eischeid, and J. Perlwitz, 2010: Regional precipitation trends:
856 Distinguishing natural variability from anthropogenic forcing. *J. Climate*, **23**, 2131–
857 2145.

858 Horel J. D. and J. M. Wallace, 1981: Planetary-Scale Atmospheric Phenomena
859 Associated with the Southern Oscillation. *Mon. Wea. Rev.*, **109**, 813–829.
860 Hurrell, J., J. Hack, D. Shea, J. Caron, and J. Rosinski, 2008: A new sea surface
861 temperature and sea ice boundary data set for the Community Atmosphere Model. *J.*
862 *Climate*, **21**, 5145–5153.
863 IPCC, 2013: Climate Change 2013: The Physical Science Basis. Contribution of Working Group
864 I to the Fifth Assessment Report of the Intergovernmental Panel on Climate Change [Stocker,
865 T.F., D. Qin, G.-K. Plattner, M. Tignor, S.K. Allen, J. Boschung, A. Nauels, Y. Xia, V. Bex
866 and P.M. Midgley (eds.)]. Cambridge University Press, Cambridge, United Kingdom and New
867 York, NY, USA, 1535 pp, doi:10.1017/CBO9781107415324.
868 Johnson, N. C., 2013: How Many ENSO Flavors Can We Distinguish? *J. Climate*, **26**,
869 4816–4827. doi: http://dx.doi.org/10.1175/JCLI-D-12-00649.1
870 Kalnay, E., et al., 1996: The NCEP/NCAR 40-year reanalysis project, *Bull. Am.*
871 *Meteorol. Soc.*, **77**, 437–471.
872 Kao, H.-Y*., and* J.-Y. Yu, 2009: Contrasting eastern-Pacific and central-Pacific types of
873 ENSO*, J. Climate,* 22*,* 615–632*, doi:*10.1175/2008JCLI2309.1.
874 Kay, J. E., Deser, C., Phillips, A., Mai, A., Hannay, C., Strand, G., Arblaster, J., Bates,
875 S., Danabasoglu, G., Edwards, J., Holland, M. Kushner, P., Lamarque, J.-F.,
876 Lawrence, D., Lindsay, K., Middleton, A., Munoz, E., Neale, R., Oleson, K., Polvani,
877 L., and M. Vertenstein, 2015: The Community Earth System Model (CESM) Large
878 Ensemble Project: A Community Resource for Studying Climate Change in the
879 Presence of Internal Climate Variability, *Bulletin of the American Meteorological*
880 *Society*, doi:10.1175/BAMS-D-13-00255.1 (in press)

881 Kim, S. T., W. Cai, F.-F. Jin, A. Santoso, L. Wu, E. Guilyardi, and S.-I. An, 2014:
882 Response of El Niño sea surface temperature variability to greenhouse warming. *Nat.*
883 *Climate Change*, **4**, 786–790, doi:10.1038/nclimate2326.
884 Kug, J.-S., F.-F. Jin, *and* S.-I. An, 2009*:* Two types of El Niño events: Cold Tongue El
885 Niño and Warm Pool El Niño*, J. Climate,* 22*,* 1499–1515*,*
886 *doi:*10.1175/2008JCLI2624.1.
887 Kumar, A., Q. Zhang, P. Peng, and B. Jha, 2005: SST-Forced Atmospheric Variability in
888 an Atmospheric General Circulation Model. *J. Climate*, **18**, 3953–3967.

889 Larkin, N. K.*, and* D. E. Harrison*,* 2005*:* Global seasonal temperature and precipitation
890 anomalies during El Niño autumn and winter*, Geophys. Res. Lett.*, 32*, L16705,*
891 *doi:*10.1029/2005GL022860.

892 Mantua, N. J., S. R. Hare, Y. Zhang, J. Wallace, and R. C. Francis, 1997: A Pacific
893 interdecadal climate oscillation with impacts on salmon production. *Bull. Amer.*
894 *Meteor. Soc.*, **78,** 1069–1079.

895 Meehl, G. A., and Coauthors, 2013: Climate change projections in CESM1 (CAM5)
896 compared to CCSM4. *J. Climate*, **26**, 6287–6308, doi:10.1175/JCLI-D-12-00572.1.
897 Mo, K. C. and R. E. Livezey, 1986: Tropical-Extratropical Geopotential Height
898 Teleconnections during the Northern Hemisphere Winter. *Mon. Wea. Rev.*, **114**, 2488–
899 2515.
900 Neale, R. B., and Coauthors, 2010: Description of the NCAR Community Atmosphere
901 Model (CAM 4.0). NCAR Tech. Note NCAR/TN-485+STR, 212 pp.

902 Neale, R. B., and Coauthors, 2012: Description of the NCAR Community Atmosphere
903 Model (CAM 5.0). NCAR Tech. Note NCAR/TN-486+STR, 274 pp.
904 Palmer, T. N., and D. A. Mansfield, 1986a: A study of wintertime circulation anomalies
905 during past El Niño events using a high resolution general circulation model: I:
906 Influence of model climatology. *Quart. J. Roy. Meteor. Soc.*, **112,** 613–638.
907 Palmer, T. N., and D. A. Mansfield, 1986b: A study of wintertime circulation anomalies
908 during past El Niño events using a high resolution general circulation model: II:
909 Variability of the seasonal mean response. *Quart. J. Roy. Meteor. Soc.*, **112,** 639–660.
910 Penland, C., and P. D. Sardeshmukh, 1995: The optimal growth of tropical sea surface
911 temperature anomalies. *J. Climate*, **8,** 1999–2024.
912 Perlwitz, J., M. P. Hoerling, and R. Dole, 2015: Arctic Tropospheric Warming: Causes
913 and Linkages to Lower Latitudes. *J. Climate*, **28**, 2154–2167. doi:
914 http://dx.doi.org/10.1175/JCLI-D-14-00095.1
915 Roeckner, E., and Coauthors, 1996: The atmospheric general circulation model
916 ECHAM4: Model description and simulation of present-day climate. Max-Planck-
917 Institut fur Meteorologie Rep. 218, Hamburg, Germany, 90 pp.
918 Saha, S., and Coauthors, 2014: The NCEP Climate Forecast System version 2. *J. Climate*,
919 **27**, 2185–2208, doi:10.1175/JCLI-D-12-00823.1.
920 Seager, R., M. Hoerling, S. Schubert, H. Wang, B. Lyon, A. Kumar, J. Nakamura, and N.
921 Henderson; 2014: Causes and predictability of the 2011-14 California drought. Report
922 of the NOAA Drought Task Force, doi:10.7289/V58K771F, 40 pp., [Available at
923 *http://docs.lib.noaa.gov/noaa_documents/OAR/CPO/MAPP/california_drought_2011-2014.pdf]*

924 Stevenson, S. L., 2012: Significant changes to ENSO strength and impacts in the twenty-
925 first century: Results from CMIP5. *Geophys. Res. Lett.,***39,** L17703,
926 doi:10.1029/2012GL052759.
927 Takahashi, K., A. Montecinos, K. Goubanova, and B. Dewitte, 2011: ENSO regimes:
928 Reinterpreting the canonical and Modoki El Niño. *Geophys. Res. Lett.*, **38**, L10704,
929 doi:10.1029/2011GL047364.
930 Ting, M., and P. D. Sardeshmukh, 1993: Factors determining the extratropical response
931 to equatorial diabatic heating anomalies. J. *Atmos. Sci.* , **50**, 907-918.
932 Trenberth, K. E., and D. P. Stepaniak, 2001: Indices of El Niño Evolution. *J. Climate*, **14**,
933 1697–1701.
934 Trenberth, K. E., 1993: The different flavors of El Niño. *Proc. 18th Annual Climate*
935 *Diagnostics Workshop*, Boulder, CO., National Oceanic and Atmospheric
936 Administration, 50-53.
937 Trenberth, K. E., G. W. Branstator, D. Karoly, A. Kumar, N.-C. Lau, and C. Ropelewski,
938 1998: Progress during TOGA in understanding and modeling global teleconnections
939 associated with tropical sea surface temperatures. *J. Geophys. Res.*, **103**, 14 291–14
940 324.
941 Vimont, D. J., D. S. Battisti, and A. C. Hirst, 2001: Footprinting: A seasonal link between
942 the tropics and mid-latitudes. *Geophys. Res. Lett.*, **28**, 3923–3926.
943 Vimont, D. J., D. S. Battisti, and A. C. Hirst, 2003a: The seasonal footprinting
944 mechanism in the CSIRO general circulation models. *J. Climate*, **16**, 2653–2667.
945 Vimont, D. J., J. M. Wallace, and D. S. Battisti, 2003b: The seasonal footprinting
946 mechanism in the Pacific: Implications for ENSO. *J. Climate*, **16**, 2668–2675.

947 Wang, S.-Y., L. Hipps, R. R. Gillies, *and* J.-H. Yoon, 2014*:* Probable causes of the
948 abnormal ridge accompanying the 2013–2014 California drought: ENSO precursor
949 and anthropogenic warming footprint*, Geophys. Res. Lett.,* **41***,* 3220–3226*,*
950 *doi:*10.1002/2014GL059748.
951 Wittenberg, A. T., 2009: Are historical records sufficient to constrain ENSO simulations?
952 *Geophys*. *Res*. *Lett*., 36, L12702, doi:10.1029/2009GL038710.
953 Yeh, S.-W., J.-S. Kug, B. Dewitte, M.-H. Kwon, B. P. Kirtman, *and* F.-F. Jin, 2009*:* El
954 Niño in a changing climate*, Nature,* 461*,* 511–514*, doi:*10.1038/nature08316.

955 Yeh, S.-W., B. P. Kirtman, J.-S. Kug, W. Park, and M. Latif, 2011: Natural variability of
956 the central Pacific El Niño event on multi-centennial timescales, *Geophys*. *Res*. *Lett*., 38,
957 L02704, doi:10.1029/2010GL045886.

958 Yu, J.-Y., *and* H.-Y. Kao, 2007*:* Decadal changes of ENSO persistence barrier in SST
959 and ocean heat content indices: 1958–2001*, J. Geophys. Res.,* 112*, D13106,*
960 *doi:*10.1029/2006JD007654.
961 Yu, J.-Y., Y. Zou, S. T. Kim, *and* T. Lee, 2012*:* The changing impact of El Niño on US
962 winter temperatures*, Geophys. Res. Lett*., 39*, L15702, doi:*10.1029/2012GL052483.
963 Zhang, T., D.-Z. Sun, R. Neale, and P. J. Rasch, 2009: An evaluation of ENSO
964 asymmetry in the Community Climate System Models: A view from the subsurface. *J.*
965 *Climate*, **22**, 5933–5961.
966 Zhang, T., J. Perlwitz, and M. P. Hoerling, 2014: What is responsible for the strong
967 observed asymmetry in teleconnections between El Niño and La Niña? *Geophys. Res.*
968 *Lett.*, **41**, 1019–1025, doi:10.1002/2013GL058964.

969 Zhang, T., and D.-Z. Sun, 2014: ENSO Asymmetry in CMIP5 Models. *J. Climate*, **27**,
970 4070-4093, doi:10.1175/JCLI-D-13-00454.1.
971 Zhang, Y., J. M. Wallace, and D. S. Battisti, 1997: ENSO-like interdecadal variability:
972 1900–1993. *J. Climate*, **10,** 1004–1020.
973
974

975 **Figure Captions**

976

977 Figure 1. (left) The spatial pattern and (right) standardized PC time series of the leading
978 two EOFs of GFSv2 simulated 50-member ensemble mean winter (DJF) season 500-hPa
979 heights. The analysis is computed over the 20^{o}N-90^{o}N domain for 1979/80 through
980 2013/14. The EOF patterns are shown as the regressions of the heights onto the
981 standardized PC time series, and drawn at the interval of 5 meter for a 1 standardized
982 departure of PC index.

983

984 Figure 2. The scatter relationship between observed tropical Pacific SST indices and the
985 PC indices from GFSv2 simulations shown in Figure 1. The top panel shows the
986 relationship between N3.4 (SST anomalies in the Niño 3.4 region) standardized index and
987 PC1 index, and the bottom panel shows the relationship between TNI (Trans-Niño Index)
988 standardized index and PC2 index. The observational SST data used in the calculations
989 are from Hurrell et al. (2008).

990

991 Figure 3. (left) The observed regression patterns of winter (DJF) season 500-hPa heights
992 onto (top) the Niño3.4 SST anomalies and onto (bottom) TNI index over the 20^{o}N-90^{o}N
993 domain for the period of 1979-2014. (right) Corresponding regression patterns of GFSv2
994 simulated 50-member ensemble mean winter (DJF) season 500-hPa heights. The
995 observational estimates are based on NCEP/NCAR height fields and Hurrell et al. (2008)
996 SST data. The contour interval is 5 meter per degree Celsius for top panels and 5 meter
997 per standard unit for bottom panels.

998 Figure 4. The scatter relationship between PC1 index and PC2 index from GFSv2
999 simulations shown in Figure 1.
1000
1001 Figure 5. (left) The composite DJF anomalies of (first row) Northern Hemisphere 500-
1002 hPa height, (second row) tropical SST, (third row) North American surface temperature,
1003 (fourth row) tropical precipitation, and (fifth row) North American precipitation for 7
1004 strongest cases with positive PC1 values from GFSv2 simulations shown in Figure 4.
1005 (right) Corresponding anomalies for 7 strongest cases with negative PC1 values shown in
1006 Figure 4. The contour interval of height fields in the first row is 10 meter.
1007
1008 Figure 6. The sum between composite DJF anomalies of 7 strongest cases with positive
1009 PC1 values (left panels of Figure 5) and composite DJF anomalies of 7 strongest cases
1010 with negative PC1 values (right panels of Figure 5). The contour interval of height fields
1011 in the first row is 10 meter.
1012
1013 Figure 7. (left) The composite DJF anomalies of (first row) Northern Hemisphere 500-
1014 hPa height, (second row) tropical SST, (third row) North American surface temperature,
1015 (fourth row) tropical precipitation, and (fifth row) North American precipitation for 7
1016 strongest cases with positive PC2 values from GFSv2 simulations shown in Figure 4.
1017 (right) Corresponding anomalies for 7 strongest cases with negative PC2 values shown in
1018 Figure 4. The contour interval of height fields in the first row is 10 meter.
1019

1020 Figure 8. Top panels show (left) the spatial pattern and (right) standardized PC time
1021 series of EOF3 of GFSv2 simulated 50-member ensemble mean winter (DJF) season 500-
1022 hPa heights. The bottom panels show (left) the spatial pattern and (right) standardized PC
1023 time series of the leading EOF of 50-member ensemble mean winter (DJF) season 500-
1024 hPa heights in coupled model runs which include 20 runs from CCSM4 and 30 runs from
1025 CESM1. The analysis is computed over the 20^{o}N-90^{o}N domain for 1979/80 through
1026 2013/14. The EOF patterns are shown as the regressions of the heights onto the
1027 standardized PC time series, and drawn at the interval of 1 meter for a 1 standardized
1028 departure of PC index.
1029
1030 Figure 9. (Top) The ratio of forced component to the total variance of winter (DJF)
1031 seasonally averaged 500-hPa height for 1979/80 through 2013/14 in GFSv2 AMIP runs.
1032 The results are shown for (left) the NH polar cap to 20^{o}N, and for (right) the global
1033 domain. (Bottom) corresponding results from coupled model runs which are the
1034 combinations of the runs from CCSM4 and CESM1. The contour interval is 0.05 for left
1035 panels and 0.2 for right panels. Forced variability is computed from the variance of
1036 ensemble means. Total variability is computed from the concatenated time series of the
1037 individual members. For two coupled models, the total variability is computed for each
1038 separately, and then averaged.
1039
1040 Figure 10. The ratio of the leading three EOFs of forced component to the total variance
1041 of winter (DJF) seasonally averaged 500-hPa height for 1979/80 through 2013/14 in
1042 GFSv2 AMIP runs. The height anomalies projecting on different modes can be computed

1043 as the scalar product of different EOF patterns and the associated PC time series. The
1044 contour interval is 0.05.
1045
1046 Figure 11. The trend pattern of EOF1, the sum of EOF1 and EOF3, and the trend pattern
1047 of ensemble mean of winter (DJF) season 500-hPa heights from GFSv2 AMIP runs over
1048 the 20°N-90°N domain for 1979/80 through 2013/14. The observed trend pattern is
1049 shown in lower right. The trend patterns of EOF1 and EOF3 are obtained by the product
1050 between the EOF pattern and the total trend of the corresponding PC time series (the total
1051 trend is -1.09 standardized unit for PC1 and 2.0 standardized unit for PC3) shown in the
1052 top panels of Figure 1 and Figure 8, respectively. The contour interval is 5 meter.
1053
1054 Figure A1. The spatial pattern of the leading three EOFs of winter (DJF) season 500-hPa
1055 heights from (left) observations, (middle) the concatenation of all 50 AMIP runs of
1056 GFSv2 and (right) a 100-yr-long GFSv2 climatological run in which the model is driven
1057 by observed SST climatology. Note that the model data used here are not ensemble
1058 means. The observational estimate is based on NCEP reanalysis for 1979/80 through
1059 2013/14. The analysis is computed over the 20°N-90°N domain. The EOF patterns are
1060 shown as the regressions of the heights onto the standardized PC time series, and drawn
1061 at the interval of 5 meter for a 1 standardized departure of PC index.
1062
1063 Figure B1. (left) The spatial pattern and (right) standardized PC time series of the leading
1064 two EOFs of winter (DJF) season 500-hPa ensemble mean heights from GFSv2 AMIP
1065 runs and ECHAM4.5 AMIP runs for the common period of 1979-2003. The analysis is

computed over the 20°N-90°N domain based on 50-member ensemble mean from GFSv2 model and 85-member ensemble mean from ECHAM4.5 model. The EOF patterns are shown as the regressions of the heights onto the standardized PC time series, and drawn at the interval of 5 meter for a 1 standardized departure of PC index.

Figure C1. Ensemble mean of (top left) the spatial pattern and (top right) standardized PC time series of the leading EOF of winter (DJF) season 500-hPa heights averaged over 50 individual coupled runs which include 20 runs from CCSM4 and 30 runs from CESM1. (bottom) Probability distribution function (PDF) for the EOF1 pattern congruence between individual coupled runs (indicated by short red lines) and NCEP reanalysis shown in Figure A1. The EOF analysis is computed over the 20°N-90°N domain for 1979/80 through 2013/14 and pattern congruence analysis is computed over the same domain. The EOF patterns are shown as the regressions of the heights onto the standardized PC time series, and drawn at the interval of 5 meter for a 1 standardized departure of PC index. The PDF is a nonparametric curve constructed using the R software program, which utilizes a kernel density estimation and a Gaussian smoother.

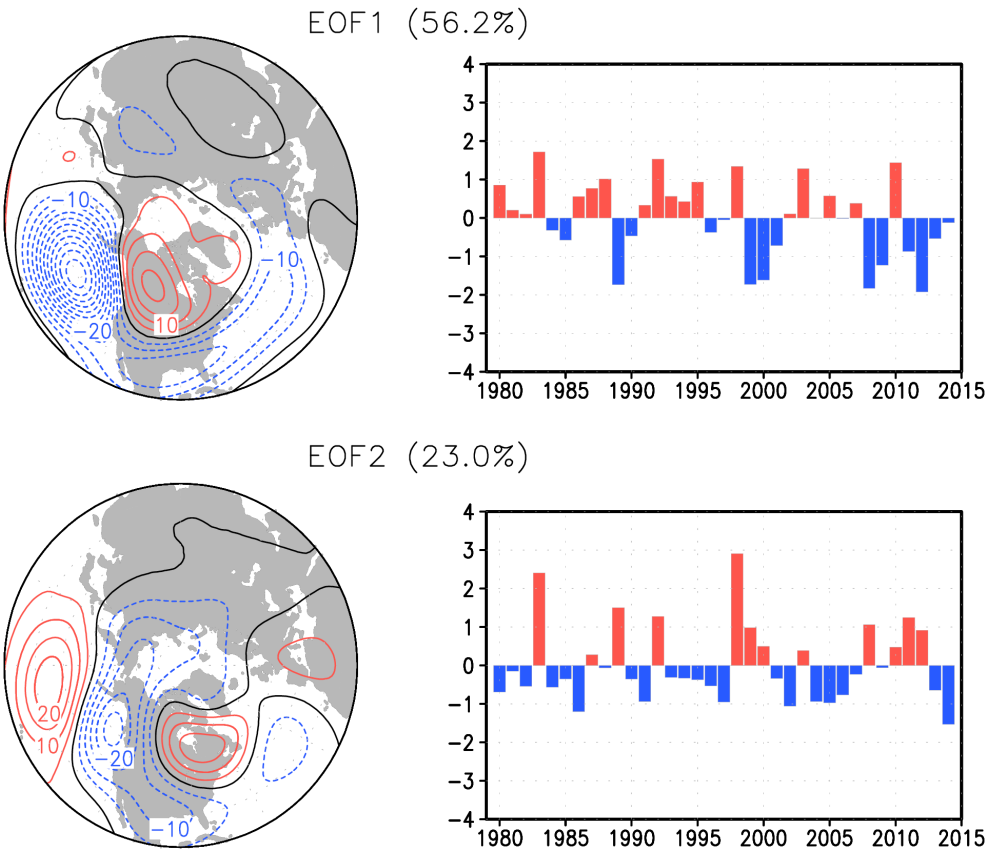

Figure 1. (left) The spatial pattern and (right) standardized PC time series of the leading two EOFs of GFSv2 simulated 50-member ensemble mean winter (DJF) season 500-hPa heights. The analysis is computed over the 20°N-90°N domain for 1979/80 through 2013/14. The EOF patterns are shown as the regressions of the heights onto the standardized PC time series, and drawn at the interval of 5 meter for a 1 standardized departure of PC index.

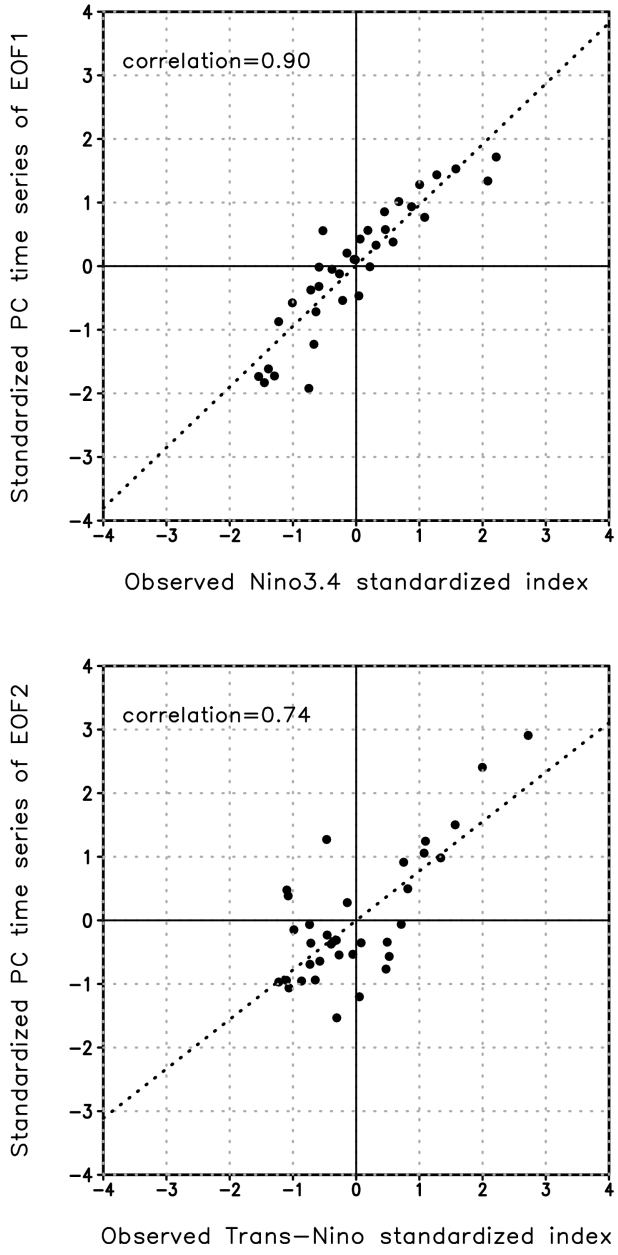

Figure 2. The scatter relationship between observed tropical Pacific SST indices and the PC indices from GFSv2 simulations shown in Figure 1. The top panel shows the relationship between N3.4 (SST anomalies in the Niño 3.4 region) standardized index and PC1 index, and the bottom panel shows the relationship between TNI (Trans-Niño Index) standardized index and PC2 index. The observational SST data used in the calculations are from Hurrell et al. (2008).

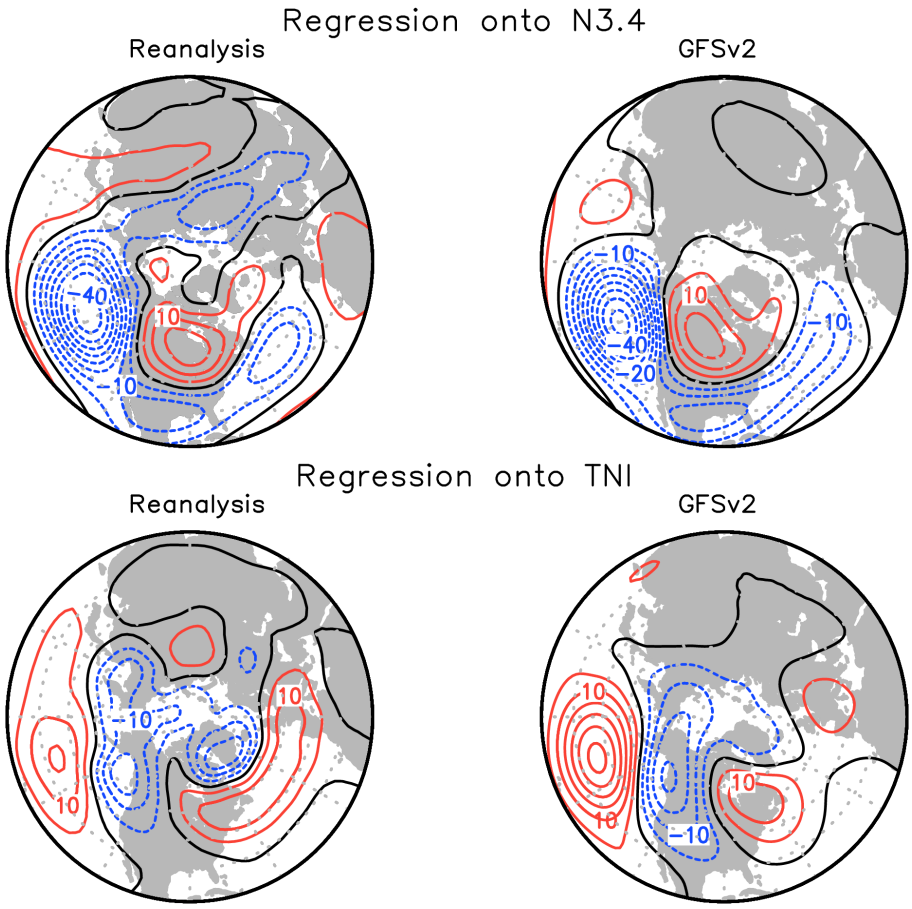

Figure 3. (left) The observed regression patterns of winter (DJF) season 500-hPa heights onto (top) the Niño3.4 SST anomalies and onto (bottom) TNI index over the 20°N-90°N domain for the period of 1979-2014. (right) Corresponding regression patterns of GFSv2 simulated 50-member ensemble mean winter (DJF) season 500-hPa heights. The observational estimates are based on NCEP/NCAR height fields and Hurrell et al. (2008) SST data. The contour interval is 5 meter per degree Celsius for top panels and 5 meter per standard unit for bottom panels.

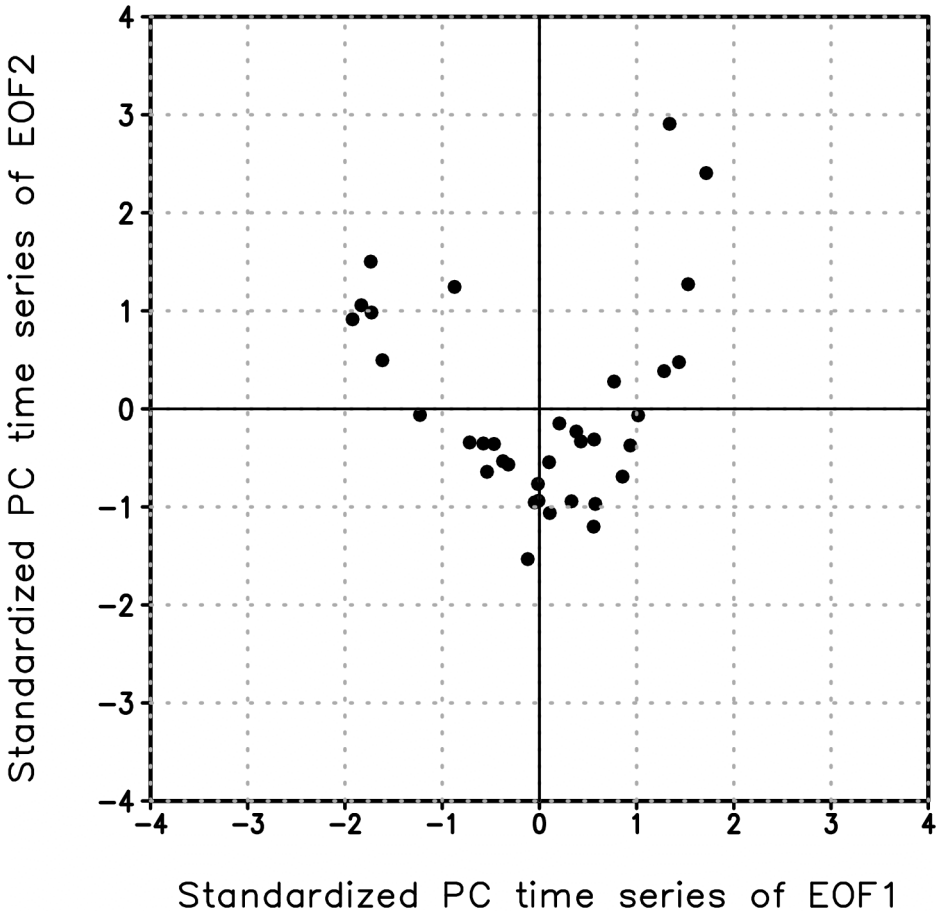

Figure 4. The scatter relationship between PC1 index and PC2 index from GFSv2 simulations shown in Figure 1.

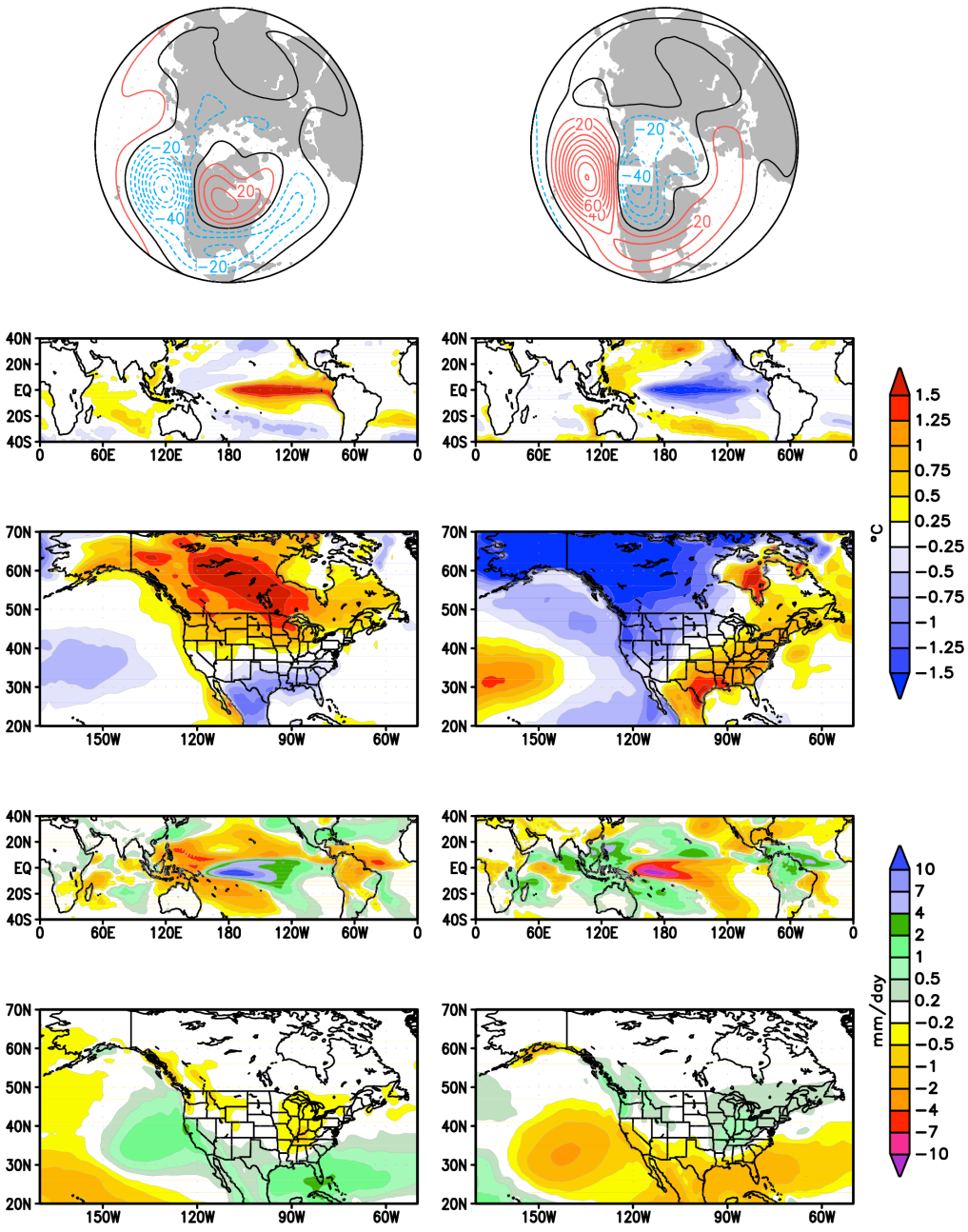

Figure 5. (left) The composite DJF anomalies of (first row) Northern Hemisphere 500-hPa height, (second row) tropical SST, (third row) North American surface temperature, (fourth row) tropical precipitation, and (fifth row) North American precipitation for 7 strongest cases with positive PC1 values from GFSv2 simulations shown in Figure 4. (right) Corresponding anomalies for 7 strongest cases with negative PC1 values shown in Figure 4. The contour interval of height fields in the first row is 10 meter.

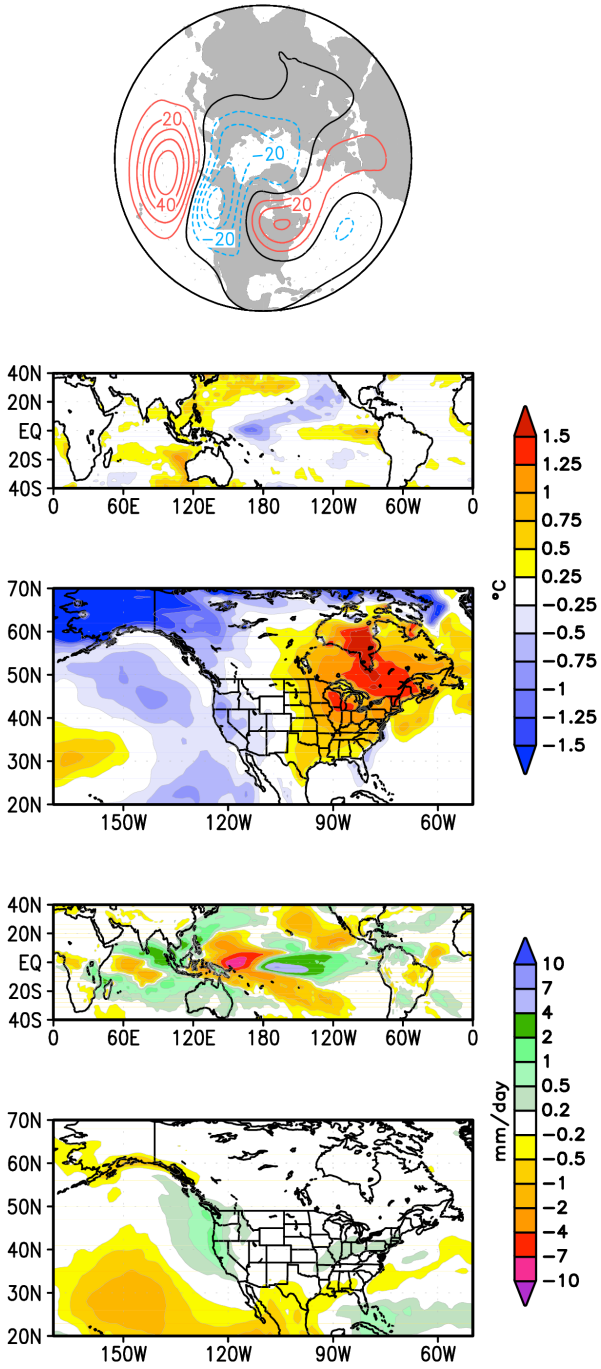

Figure 6. The sum between composite DJF anomalies of 7 strongest cases with positive PC1 values (left panels of Figure 5) and composite DJF anomalies of 7 strongest cases with negative PC1 values (right panels of Figure 5). The contour interval of height fields in the first row is 10 meter.

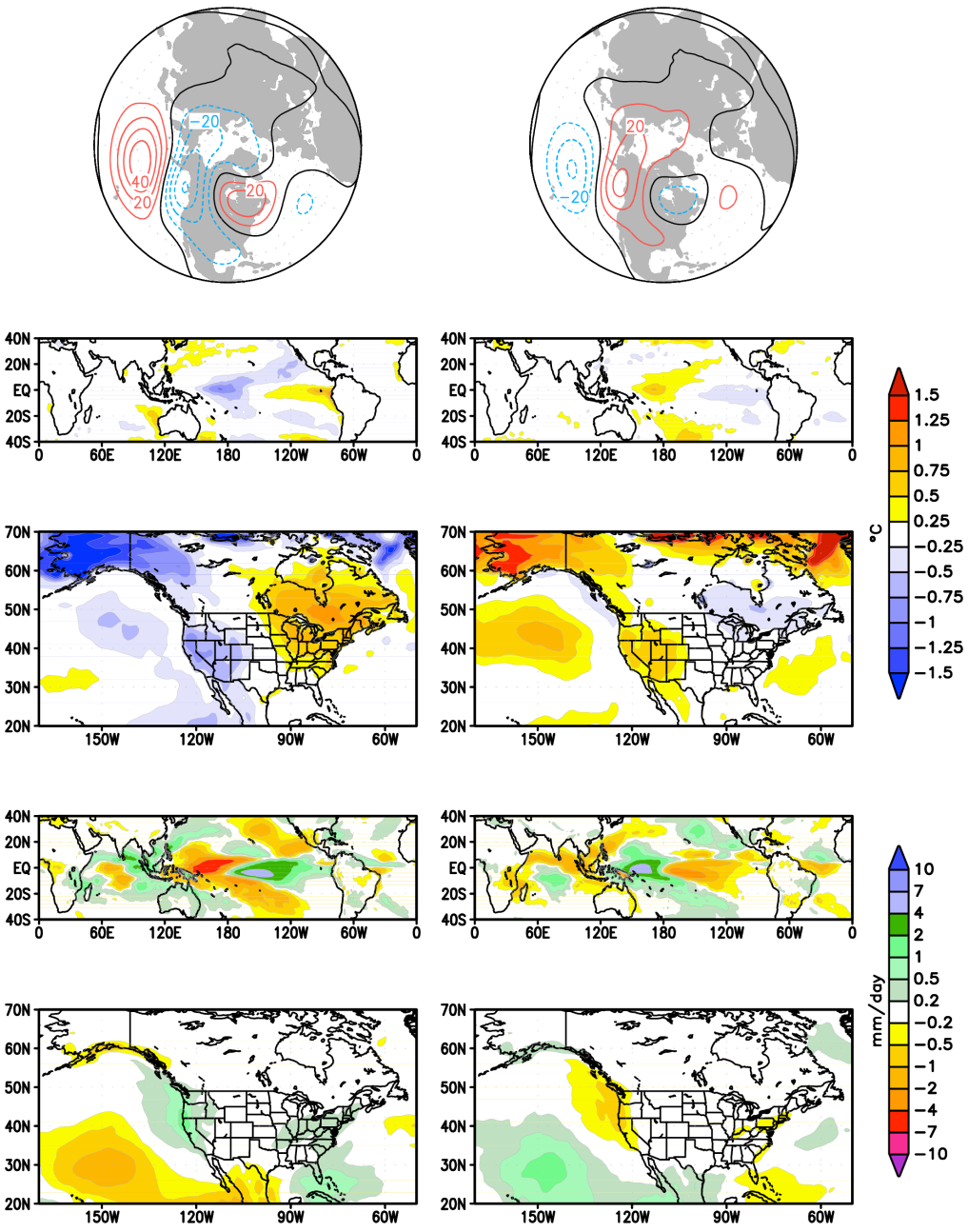

Figure 7. (left) The composite DJF anomalies of (first row) Northern Hemisphere 500-hPa height, (second row) tropical SST, (third row) North American surface temperature, (fourth row) tropical precipitation, and (fifth row) North American precipitation for 7 strongest cases with positive PC2 values from GFSv2 simulations shown in Figure 4. (right) Corresponding anomalies for 7 strongest cases with negative PC2 values shown in Figure 4. The contour interval of height fields in the first row is 10 meter.

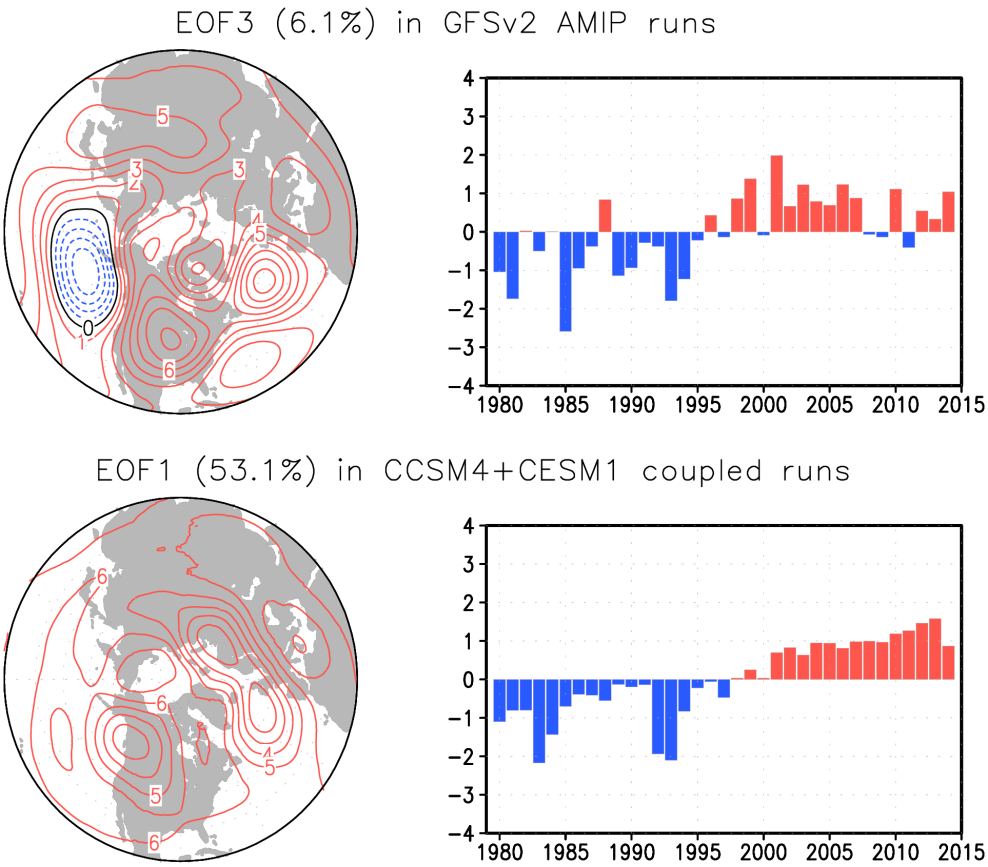

Figure 8. Top panels show (left) the spatial pattern and (right) standardized PC time series of EOF3 of GFSv2 simulated 50-member ensemble mean winter (DJF) season 500-hPa heights. The bottom panels show (left) the spatial pattern and (right) standardized PC time series of the leading EOF of 50-member ensemble mean winter (DJF) season 500-hPa heights in coupled model runs which include 20 runs from CCSM4 and 30 runs from CESM1. The analysis is computed over the 20°N-90°N domain for 1979/80 through 2013/14. The EOF patterns are shown as the regressions of the heights onto the standardized PC time series, and drawn at the interval of 1 meter for a 1 standardized departure of PC index.

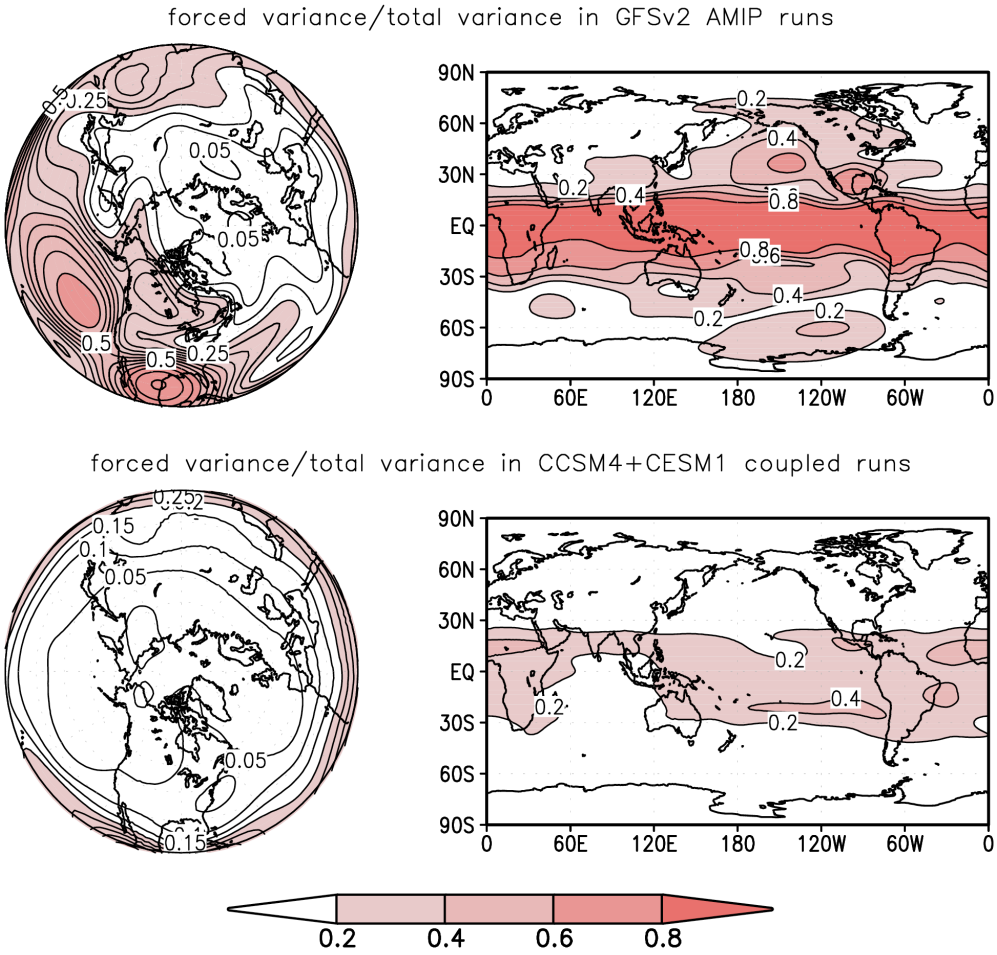

Figure 9. (Top) The ratio of forced component to the total variance of winter (DJF) seasonally averaged 500-hPa height for 1979/80 through 2013/14 in GFSv2 AMIP runs. The results are shown for (left) the NH polar cap to 20°N, and for (right) the global domain. (Bottom) corresponding results from coupled model runs which are the combinations of the runs from CCSM4 and CESM1. The contour interval is 0.05 for left panels and 0.2 for right panels. Forced variability is computed from the variance of ensemble means. Total variability is computed from the concatenated time series of the individual members. For two coupled models, the total variability is computed for each separately, and then averaged.

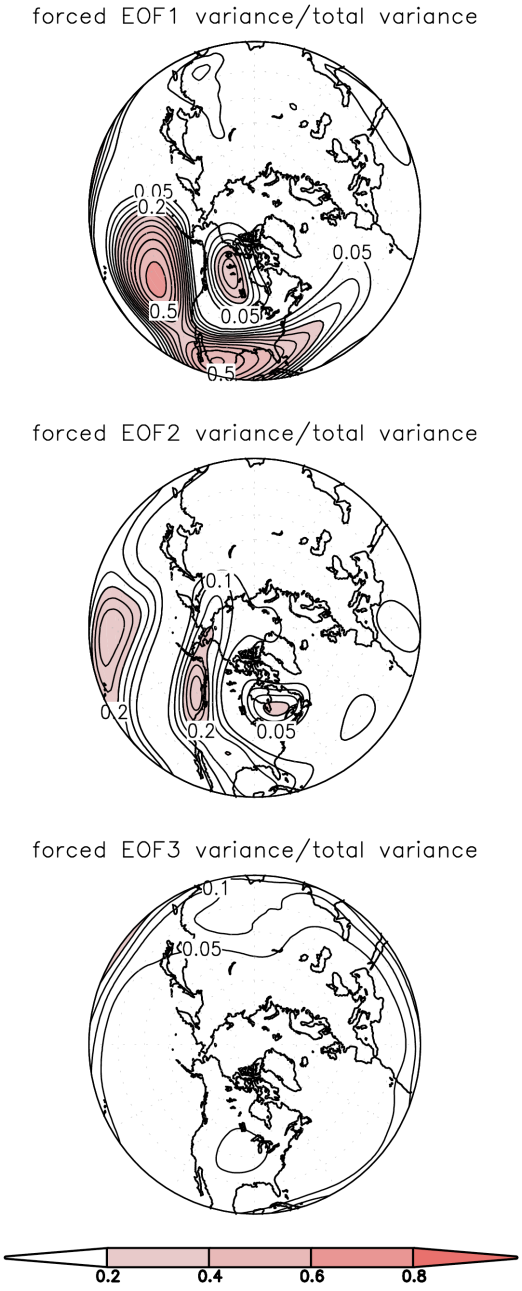

Figure 10. The ratio of the leading three EOFs of forced component to the total variance of winter (DJF) seasonally averaged 500-hPa height for 1979/80 through 2013/14 in GFSv2 AMIP runs. The height anomalies projecting on different modes can be computed as the scalar product of different EOF patterns and the associated PC time series. The contour interval is 0.05.

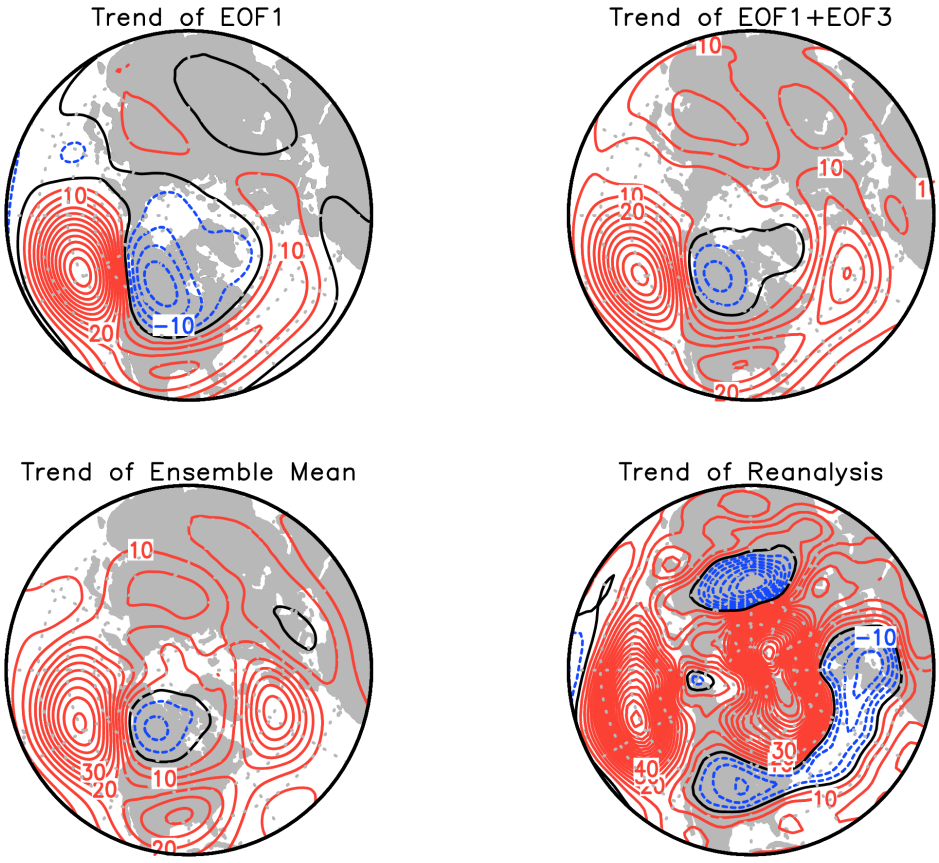

Figure 11. The trend pattern of EOF1, the sum of EOF1 and EOF3, and the trend pattern of ensemble mean of winter (DJF) season 500-hPa heights from GFSv2 AMIP runs over the 20°N-90°N domain for 1979/80 through 2013/14. The observed trend pattern is shown in lower right. The trend patterns of EOF1 and EOF3 are obtained by the product between the EOF pattern and the total trend of the corresponding PC time series (the total trend is -1.09 standardized unit for PC1 and 2.0 standardized unit for PC3) shown in the top panels of Figure 1 and Figure 8, respectively. The contour interval is 5 meter.

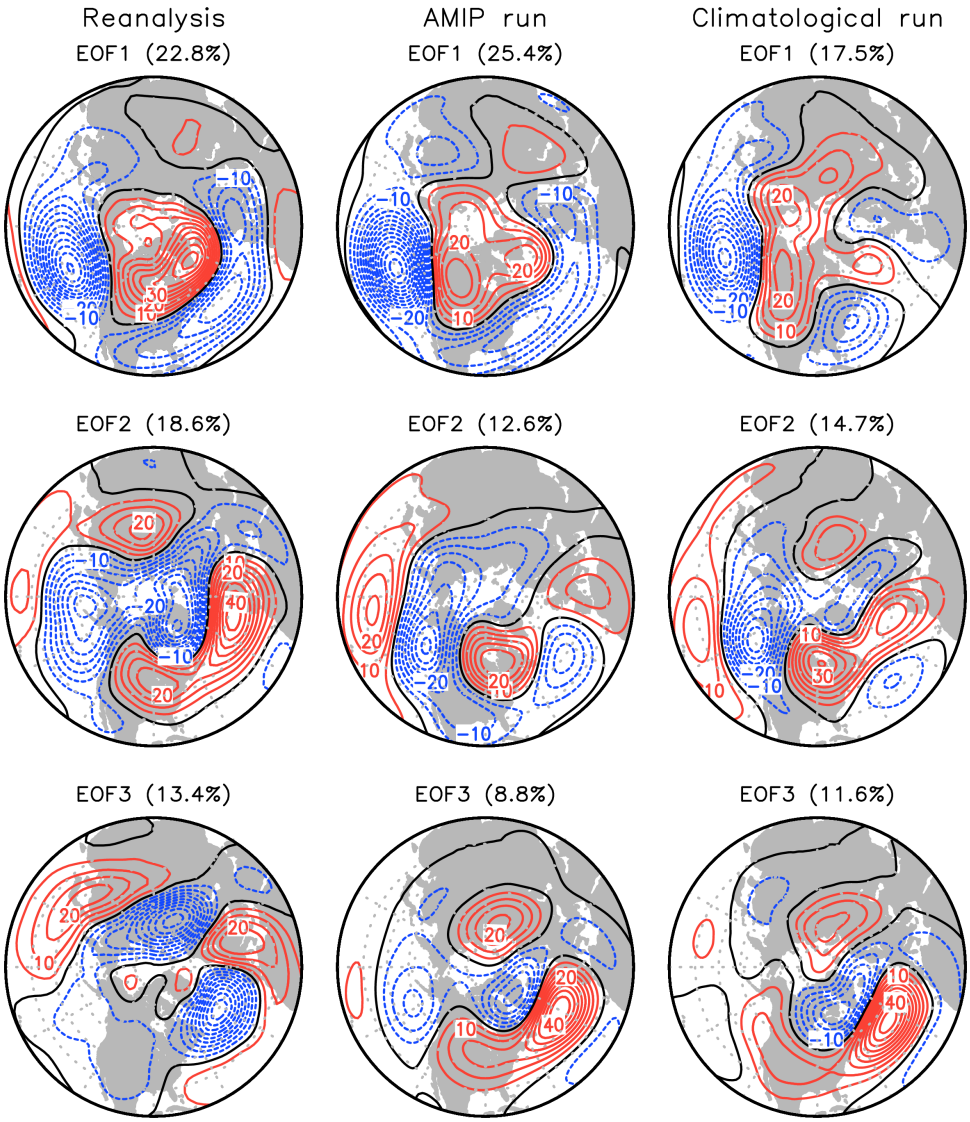

Figure A1. The spatial pattern of the leading three EOFs of winter (DJF) season 500-hPa heights from (left) observations, (middle) the concatenation of all 50 AMIP runs of GFSv2 and (right) a 100-yr-long GFSv2 climatological run in which the model is driven by observed SST climatology. Note that the model data used here are not ensemble means. The observational estimate is based on NCEP reanalysis for 1979/80 through 2013/14. The analysis is computed over the 20°N-90°N domain. The EOF patterns are shown as the regressions of the heights onto the standardized PC time series, and drawn at the interval of 5 meter for a 1 standardized departure of PC index.

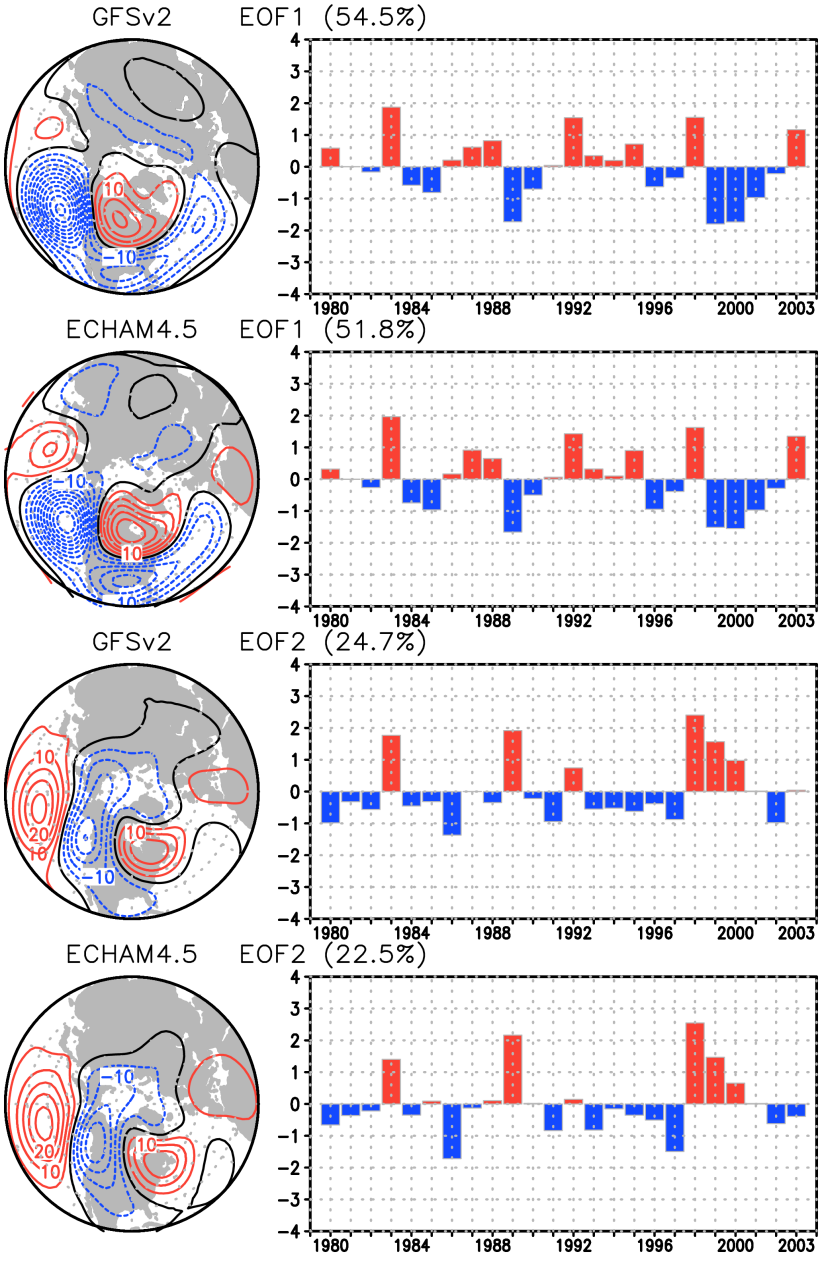

Figure B1. (left) The spatial pattern and (right) standardized PC time series of the leading two EOFs of winter (DJF) season 500-hPa ensemble mean heights from GFSv2 AMIP runs and ECHAM4.5 AMIP runs for the common period of 1979-2003. The analysis is computed over the 20°N-90°N domain based on 50-member ensemble mean from GFSv2 model and 85-member ensemble mean from ECHAM4.5 model. The EOF patterns are shown as the regressions of the heights onto the standardized PC time series, and drawn at the interval of 5 meter for a 1 standardized departure of PC index.

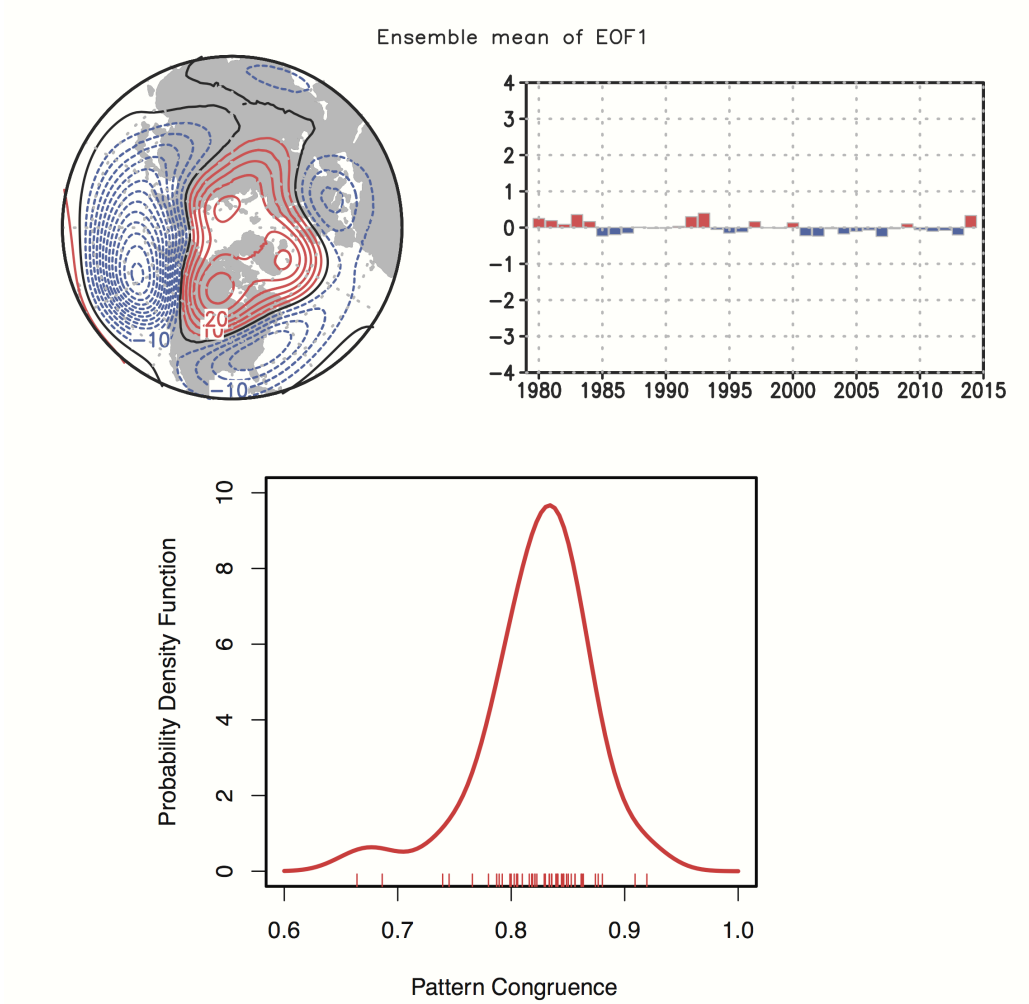

Figure C1. Ensemble mean of (top left) the spatial pattern and (top right) standardized PC time series of the leading EOF of winter (DJF) season 500-hPa heights averaged over 50 individual coupled runs which include 20 runs from CCSM4 and 30 runs from CESM1. (bottom) Probability distribution function (PDF) for the EOF1 pattern congruence between individual coupled runs (indicated by short red lines) and NCEP reanalysis shown in Figure A1. The EOF analysis is computed over the 20°N-90°N domain for 1979/80 through 2013/14 and pattern congruence analysis is computed over the same domain. The EOF patterns are shown as the regressions of the heights onto the standardized PC time series, and drawn at the interval of 5 meter for a 1 standardized departure of PC index. The PDF is a nonparametric curve constructed using the R software program, which utilizes a kernel density estimation and a Gaussian smoother.